Post-critical *SsPmp* and its Applications to Virtual Deep Seismic Sounding (VDSS)–3: Back-projection Imaging of the Crust-Mantle Boundary in a Heterogeneous Lithosphere

Tianze Liu[1] (tianze@stanford.edu), Simon L. Klemperer[1], Chunquan Yu[2,3], Jieyuan Ning[4]

1. Department of Geophysics, Stanford University
2. Seismological Laboratory, California Institute of Technology
3. Now at Department of Earth and Space Sciences, Southern University of Science and Technology
4. Institute of Theoretical and Applied Geophysics, School of Earth and Space Science, Peking University

SUMMARY

Virtual Deep Seismic Sounding (VDSS) uses the arrival time of post-critical *SsPmp* relative to the direct S wave to infer Moho depth at the *Pmp* reflection point. Due to the large offset between the virtual source and receiver, *SsPmp* is more sensitive to lateral variation of structure than near-vertical phases such as *Ps* that is used to construct conventional P receiver functions. However, the way post-critical *SsPmp* is affected by lateral variation in lithospheric structure is not well understood, and previous studies have largely assumed 1D structure when analyzing *SsPmp* waveforms. Here we present synthetic tests with various 2D models to show that lateral variation in lithospheric structure has profound effects on travel time, phase and amplitude of post-critical *SsPmp*, and that a 1D approximation is usually inappropriate when analyzing 2D data. Despite the strong effects of 2D structure on *SsPmp* travel time, we show with synthetic examples and field data from the Ordos Plateau in northern China that a simple ray-theory-based back-projection method can retrieve the geometry of the crust-mantle boundary given array observations in cases with moderate lateral variation in crust-mantle boundary and/or lithosphere-asthenosphere boundary. The success of our back-projection method indicates that ray-theory approximations are sufficient in modeling *SsPmp* travel times in the presence of moderate lateral heterogeneity. In contrast, we show that ray theory is generally insufficient in modeling *SsPmp* phase shifts in a strongly heterogeneous lithosphere due to non-planar down-going P waves incident at the crust-mantle boundary. Nonetheless, our results demonstrate the feasibility of direct imaging of the crust-mantle boundary with post-critical *SsPmp* even in the presence of 2D variation of lithospheric structure.

1. INTRODUCTION

Recent years have seen Virtual Deep Seismic Sounding (VDSS) emerging as a novel method to image the crust-mantle boundary (CMB) and being successfully applied to multiple datasets from different areas (e.g. Kang et al., 2016; Luo et al., 2018; Parker et al., 2016; Thompson et al., 2019; Tian et al., 2015; Tseng et al., 2009; Yu et al., 2012, 2016). In keeping with the first two parts of this series (Liu et al., 2018, 2019, hereafter Part 1 and 2 respectively), here we use CMB (crust-mantle boundary) to denote the boundary or geological transition from crust to mantle, and Moho to denote a seismological inference about this transition, typically given as a single depth. *SsPmp*, the seismic phase used in VDSS, originates when upcoming teleseismic S waves convert to down-going P waves at the free surface (the virtual source), which then undergo post-critical reflection at or within the CMB and finally reach the receiver (Fig. 1). In Part 1 and 2, we studied the sensitivity of *SsPmp* to lithospheric structure and developed methods to infer parameters of the crust and mantle from *SsPmp* waveforms recorded at a single station, or assuming a 1D Earth. Due to the large offset between the virtual source and receiver (typically ~120km), post-critical *SsPmp* is more sensitive to lateral variation along its ray path than near-vertical phases such as *Ps* (Fig. 1). However, previous studies have largely assumed 1D structure when analyzing *SsPmp* waveforms (e.g. Yu et al., 2012; Tseng et al., 2009; Tian et al., 2015). Yu et al. (2016) noted that lateral (2D) variation in lithospheric V_s causes travel-time differences between the up-coming S legs of *SsPmp* and *Ss* that are incorrectly included in estimated crustal thickness if a 1D approximation is used (see also Figure 11 in Part 1). Yu et al. (2016) proposed an array-based method to empirically correct for the effects of lateral V_s variation. However, when *Ss* arrival time as a function of distance deviates from the 1D prediction, the ray parameters of *Ss* and of *SsPmp* are different due to lateral heterogeneity and vary with distance in a different way from the 1D case. It is not immediately clear how this variation affects T_{VDSS}, Φ_{VDSS} and A_{VDSS} (respectively the relative arrival time, angular phase and amplitude of *SsPmp* wih respect to direct *Ss*).

Here, we present synthetic tests to demonstrate the effects of lateral heterogeneity on T_{VDSS}, Φ_{VDSS} and A_{VDSS}. In order to image the CMB with *SsPmp* in the presence of 2D variation in lithospheric structure, we propose a simple ray-theory-based back-projection method that accounts for both lateral variation in *Ss* arrival time and ray parameter. We show that our method is capable of modeling T_{VDSS} and retrieving the geometry of the CMB using observations along a

linear array. On the other hand, we show that ray-theory approximations are insufficient to model Φ_{VDSS} due to the failure of the plane-wave approximation in the presence of lateral heterogeneity. Finally, we demonstrate the success of our back-projection method in recovering an image of the dipping Moho beneath the Ordos Block, China, in a region with lateral variation in lithospheric thickness as well as crustal thickness.

2. SYNTHETIC EXAMPLES

To study the potential effects of lateral heterogeneity in the lithosphere on *SsPmp* waveforms, we use the SPECFEM2D software package to compute 2D synthetic waveforms (Komatitsch et al., 2001; Komatitsch and Vilotte, 1998; Tromp et al., 2008). Our models consist of three layers: crust, lithospheric mantle, and asthenosphere, the material properties of which are shown in the format V_p/V_s/density in Fig. 2a and are held constant across all models in this paper. The incident wave is set to be a plane S wave with incident angle of 35º (p_0 = 0.1275 s/km, $1/p_0$ =7.84 km/s) in the asthenosphere for all models (Fig 2a). Our source time function is a first-order Hermitian wavelet (first derivative of Gaussian wavelet) with dominant frequency ~0.25 Hz, similar in shape and frequency component to the source time functions of deep and intermediate-depth earthquakes that we use later (Fig. 12). We place receivers at the free surface with 10-km spacing. We then vary the geometries of the CMB (here a sharp boundary) and lithosphere-asthenosphere boundary (LAB) in the models to show their effects on *SsPmp* waveforms. Section 2.1 (Figs. 2–4 and S1) considers a sinusoidal LAB beneath a flat CMB. Section 2.2 (Figs. 6–9 and S2–3) models a sinusoidal CMB above a flat LAB. Section 2.3 (Figs. 9–10 and S4–5) studies a sinusoidal LAB beneath a sinusoidal CMB. We consider sinusoidal boundaries with CMB varying between 30 and 50 km depth (amplitude $2A$ = 20 km) and LAB varying between 80 and 200 km depth ($2A$ = 120 km). We test topographic wavelengths λ = 1200 km, 600 km and 400 km, so that for the CMB $2A/\lambda$ = 0.0167, 0.0333 and 0.0500, and for the LAB $2A/\lambda$ = 0.1, 0.2, 0.3. Average boundary dip θ_{av} is a reasonable proxy for model complexity (steeper topography causes more ray-path bending). Our models have θ_{av} = 2º, 4º and 6º respectively for the CMB, and θ_{av} = 11º, 22º and 31º for the LAB. For our models we choose the amplitude of the LAB topography to be six times the CMB topography in order to give similar variability in *Ss* travel time residuals (~1 s) for the ±60-km LAB variation and for the ±10-km CMB. This ratio of LAB-to-CMB topography is also a sensible approximation to the real earth:

in the northern Basin and Range Province of the western U.S.A. the CMB has λ = ~400 km and $2A$ = ~7 km, with θ_{av} = ~2º (Klemperer et al., 1986), while the LAB in the region shows no significant variation (Hopper and Fischer, 2018) (cf. model in Fig. 6). At the boundary between the western and the eastern North China Craton, the Moho deepens westward from 30-40 km across ~200 km (Jia et al., 2014), with θ_{av} = ~3º, while the LAB deepens westward from 80-200 km across ~600 km, with θ_{av} = ~11º (Chen et al., 2009) (cf. model in Fig. 10). At the boundary between the southern Sierra Nevada and the Basin and Range Province, the CMB has λ = ~300 km and $2A$ = ~10 km, with θ_{av} = ~4º, while the LAB varies approximately in phase with CMB and has λ = ~300 km and $2A$ = ~60 km, with θ_{av} = ~22º (Fliedner et al., 1996) (cf. model in Fig. 11). The northern Basin and Range is representative of CMB and LAB variation within one geologic province, whereas the boundaries between southern Sierra Nevada and Basin and Range, and between the eastern and western North China Craton, are representative of CMB and LAB variation between different geologic provinces, which likely have different lithosphere velocity structure not captured in our models. In our test models the LAB is set as a sharp boundary for simplicity, whereas in reality the LAB may span tens of kilometers (Fischer et al., 2010). However, for the same total velocity change across the LAB, a sharp and a transitional LAB will have the same effect on *SsPmp* waveforms. We note that the average CMB and LAB dips chosen for our smoothest (Figs. 2a, 6a, 10a) and intermediate (Figs. 3a, 7a, 11a) models are similar to the above examples, which makes them appropriate for studying the effects of lateral structural variation on real *SsPmp* waveforms. Our most extreme models (Figs. 4a, 9a, S5a) serve to demonstrate the very real limits of our methodology, albeit in circumstances not often encountered in reality.

2.1. Effects of LAB Topography

We model a flat CMB at 40 km depth, and a sinusoidal LAB varying between 80 and 200 km-depth. We vary the wavelength of the LAB from 1200 km (Fig. 2a), through 600 km (Fig. 3a), to 400 km (Fig. 4a) to test its effect on *SsPmp* waveforms.

2.1.1. Effects of gentle dips

We start with the 1200-km wavelength case, in which the average dip of the LAB is ~11º (Fig. 2a). Fig. 2b shows vertical-component waveforms (containing both P- and S-energy)

plotted against receiver locations and reduced travel times calculated with an apparent velocity of $V_{app} = 1/p_0 = 7.84$ km/s: *Ss* and *SsPmp* are clear across the profile. *Ss* arrival times oscillate around zero time due to lateral velocity variations, indicating a non-planar wave is incident at the free surface. Because the source plane wave is incident from the lower left of the model, the early (late) arrivals of *Ss* are displaced to the right of the causative high (low) velocity variations. To further align the traces, we separate the waveforms into pseudo-P (motion associated with incoming P wave) and pseudo-S (motion associated with incoming S wave) components (hereafter P and S for simplicity) with a particle-motion-analysis algorithm (Yu et al., 2013) and apply multi-component cross-correlation on the S-component waveforms, which are assumed to contain only *Ss*. We use time shifts given by multi-component cross-correlation of *Ss* to align the seismograms to the zero-crossings (peak of envelope functions for our first-order Hermitian function) of their *Ss* arrivals (Fig. 2c; note we show vertical-component not pseudo-P or -S). After alignment we observe ~1 s variation of T_{VDSS} across the profile due to the 1200 km-wavelength variation in LAB depth, which could be misinterpreted as Moho depth variation on the order of 5 km. This potential pitfall highlights the importance of correcting for lateral heterogeneity effects when converting T_{VDSS} to Moho depth (cf. Figure 11 in Part 1).

In order to better understand the behavior of the SPECFEM-modeled wavefield, we trace rays through our model and compare the ray-path distributions with the synthetic waveforms. For *Ss*, we shoot S rays with constant take-off angle of 35º from 10-km-spacing starting points at the bottom of the model. The S rays undergo Snell's-Law refraction and reflection en route to the surface (Fig. 2h). We compute the "theoretical *Ss* ray parameter" of each ray from its incident angle at the free surface and plot it at its free-surface (i.e. virtual-source) location (gray curve in Fig. 2d). As a result of the lateral variation in velocity structure, the *Ss* ray parameters vary between 0.1258 and 0.1301 s/km (Fig. 2d). Alternatively, we can compute the "apparent *Ss* ray parameter" at the free surface by differentiating *Ss* arrival time with respect to distance. Our apparent *Ss* ray parameters agree well with the theoretical *Ss* ray parameters (Fig. 2d), which indicates that in this case apparent *Ss* ray parameters directly calculated from observed waveforms are equivalent to theoretical *Ss* ray parameters that can only be derived if the velocity structure is known. After ray-tracing for *Ss*, we trace down-going P rays from the free-surface locations where each *Ss* ray terminates and let each P ray have the same ray parameter as the corresponding *Ss* ray because our free surface is flat. The P rays are then reflected at the CMB

and return to the surface (Fig. 2i). This is equivalent to tracing P rays with the theoretical *Ss* ray parameters, the values of which are in general unevenly distributed at the surface due to the unevenly distributed *Ss* rays. An alternative way to compute *Pmp* ray paths is to trace the P rays with the apparent *Ss* ray parameters, which in our case are evenly distributed due to constant station spacing (Fig. 2j). The *Pmp* ray paths traced with the theoretical *Ss* ray parameters better account for *SsPmp* amplitude variation, because they incorporate the uneven distribution of *Ss* rays at the surface that represents the distribution of *Ss* energy at the surface. However, we cannot derive the theoretical *Ss* ray parameters without knowing the true velocity model, so ray tracing for field data can only be conducted with apparent *Ss* ray parameters. Nonetheless, it is instructive to compute ray paths with both methods throughout this paper. In our 1200-km-wavelength case the *Pmp* rays traced with the two methods are almost identical and almost uniformly spaced (Figs. 2i, j), because the distribution of *Ss* rays is almost uniform at the surface (Fig. 2h).

In this model with only LAB topography, p_{VDSS}, the ray parameter of the *SsPmp* ray, is equal to the *Ss* ray parameter p_{Ss} and varies along the profile. It is expected that Φ_{VDSS} also changes along the profile due to its sensitivity to ray parameters in 1D structure (Part 1). To test whether our relation between p_{VDSS} and Φ_{VDSS} in 1D still holds in the presence of 2D variation, we measure Φ_{VDSS} from our synthetic waveforms (apparent Φ_{VDSS}; thin black curve in Fig. 2e) to compare with Φ_{VDSS} predicted with ray-tracing (theoretical Φ_{VDSS}; thick grey curve in Fig. 2e). We measure apparent Φ_{VDSS} by minimizing the root-mean-square misfit between observed *SsPmp* and a synthetic *SsPmp* computed by applying different phase-shifts to the source wavelet (Part 2). We align the synthetic and observed *SsPmp* with cross-correlation before calculating the misfit. In contrast we calculate the theoretical Φ_{VDSS} from the complex reflection coefficient at the CMB, which is determined by p_{VDSS} and velocity change across the CMB under the assumption of a plane incident wave (Aki and Richards, 2002). We plot the apparent Φ_{VDSS} at the receiver locations where they were measured, and the theoretical Φ_{VDSS} values at the locations where the reflected P rays reach the free surface as predicted by the ray tracing (the VDSS surfacing points) (Fig. 2e). Minor discrepancies up to 15º between the apparent and theoretical Φ_{VDSS} (Fig. 2e) are primarily caused by the curved (non-planar) incident wave-front at the CMB. Our plane-wave approximation (theoretical Φ_{VDSS}) under-predicts apparent Φ_{VDSS} where p_{VDSS}

increases with distance (retrograde; virtual sources west of 800 km in Fig. 2d corresponding to surfacing points west of 920 km in Fig. 2e), but over-predicts apparent Φ_{VDSS} where p_{VDSS} decreases with distance (prograde; virtual sources at 800-1400 km, Fig. 2d, and surfacing points from 920-1520 km, Fig. 2e). However, teleseismic-S is prograde (ray parameter p_{Ss} decreases with increasing epicentral distance), and the slope of p_{Ss} as a function of distance (~1.6 x 10^{-5} s/km/km) is similar to the slope of ray parameter due to LAB undulation in this example (~1.4 x 10^{-5} s/km/km), so we infer that a small discrepancy should exist between our theoretical Φ_{VDSS} computed with a plane incident S wave and Φ_{VDSS} computed with a realistic teleseismic S wave, even if they have the same p_{VDSS}. To further study the effects of a curved incident S wave front, we calculate upper-mantle V_p (V_p^{um}) from apparent Φ_{VDSS} under the plane-wave assumption and plot V_p^{um} at the corresponding *Pmp* reflection points (Fig. 2f). Our inferred V_p^{um} shows up to ±1.5% deviation from the true value (8.30 km/s; Fig. 2f), small compared to the range of *Pn* velocity variation (~4.5%) in the contiguous US (Buehler and Shearer, 2017). If we use more distant teleseismic events with larger $1/p_{VDSS}$ closer to the true V_p^{um}, the error in estimated V_p^{um} is reduced because, as $1/p$ approaches V_p^{um}, Φ_{VDSS} becomes increasingly sensitive to V_p^{um} (Figure 7 in Part 1), thus a fixed error in Φ_{VDSS} causes a smaller error in V_p^{um}.

2.1.2. Moho imaging by *SsPmp* back-projection

Above, we began to explore how 2D lithospheric variations affect T_{VDSS}, Φ_{VDSS} and A_{VDSS}. We next develop a simple ray-tracing-based back-projection method to image CMB geometry from observed *SsPmp* waveforms in a laterally heterogeneous Earth, utilizing a linear recording array. To address Φ_{VDSS} variation across the array, we correct all pseudo-P-component traces to 90º phase shift using the apparent Φ_{VDSS} (e.g. thick gray curve in Fig. 2e) before applying back-projection. Because the source wavelet used for our synthetic examples is antisymmetric, after a 90º-phase-shift the wavelet becomes symmetric, with the arrival time at its maximum. To back-project the data, we shoot P rays downward from each virtual source location x_{src} using apparent *Ss* ray parameters derived by differentiating the *Ss* arrival times that are sampled at our regular 10 km receiver spacing. For each successive possible Moho depth H sampled at 1 km interval, we compute the two-way P travel-time T_{ref} of a hypothetical horizontal reflector at that depth by:

$$T_{ref} = \frac{2H}{V_p^{av}\sqrt{1 - V_p^{av2}p_{Ss}^2}} \quad (1)$$

where V_p^{av} is the average crustal V_p and p_{Ss} is the *Ss* ray parameter (as used for the down-going P ray). For a flat Moho the location where the reflected *Pmp* ray reaches the surface (hereafter surfacing point) is:

$$x_{srf} = x_{src} + \frac{2HV_p^{av}p_{Ss}}{\sqrt{1 - V_p^{av2}p_{Ss}^2}} \quad (2)$$

where x_{src} is the spatial coordinate of the virtual source. The *Ss* differential travel time between *Ss* at the virtual source and *Ss* at the surfacing point is:

$$\Delta T_{Ss} = T_{Ss}(x_{src}) - T_{Ss}(x_{srf}) \quad (3)$$

Therefore, the travel time of *SsPmp* relative to *Ss* (T_{VDSS}) for this particular ray is:

$$T_{VDSS} = T_{ref} + \Delta T_{Ss} \quad (4)$$

We apply linear interpolation to the phase-shift-corrected pseudo-P-component traces (recorded at uniformly-spaced receivers) to find the energy at (x_{srf}, T_{VDSS}) for each calculated x_{srf} (Eqn. 2), and place it at depth H vertically below the midpoint between the virtual-source location and the surfacing point. To account for finite-frequency effects, we laterally smear the energy of each ray with a Gaussian function of standard deviation σ equal to the Fresnel zone radius at the corresponding depth (for our 4-s period source wavelet, $\sigma \sim$ 30 km for H = 40 km). We repeat this procedure for the P ray from every virtual-source location to form the final image (Figs. 2g, k). Because the maximum amplitude on each phase-shift-corrected trace is at T_{VDSS} we pick the maximum amplitude on each column of the image as the estimated Moho depth at that location (solid black curve in Fig. 2k). The resulting back-projection image shows the Moho image at the correct CMB depth along the profile (Figs. 2g, k). We also compute the back-projection image with a constant *Ss* ray parameter $p = p_0 = 0.1275$ s/km, which is equivalent to back-projection with the 1D travel-time equation for *SsPmp*:

$$T_{VDSS} = 2H\sqrt{\frac{1}{V_p^{av2}} - p_0^2} \quad (6)$$

This procedure gives the uncorrected Moho depth estimates (black dashed curve in Fig. 2k), which show apparent variation of Moho depth across the profile, an artifact caused by lateral

variation in the mantle. Thus, the black dashed curve represents the Moho depth that has been interpreted using existing methods, and is likely to include significant errors in areas where LAB and CMB topography are inferred (e.g. Yu et al., 2012, Tian et al., 2015). This phenomenon emphasizes the importance of incorporating *Ss* ray parameter (hence travel-time) variation in *SsPmp*-waveform analysis.

2.1.3. Additional effects of steeper dips

We next reduce the LAB wavelength to 600 km and repeat the process (Fig. 3). The average dip of the LAB is now ~22º (Fig 3a). The resulting *Ss* and *SsPmp* arrival times show stronger variation compared with the 1200 km-wavelength case (Figs. 3b, c). As a result of the stronger *Ss* arrival time variation, the apparent ray parameter also varies more strongly than the 1200 km-wavelength case (thin black curve in Fig. 3d). The *Ss* rays are slightly denser at ~980 and ~1580 km than elsewhere due to the focusing effects of a shallow LAB (Fig. 3i). The theoretical *Ss* ray parameters computed with ray tracing (thick gray curve in Fig. 3d) agree well with the apparent *Ss* ray parameters (thin black curve in Fig. 3d). We then trace *Pmp* rays with the apparent and theoretical *Ss* ray parameters, finding increased *Pmp* ray density at ~1100 and ~1700 km for both the rays traced with theoretical and apparent ray parameters, with the former having stronger ray density variation than the latter (Figs. 3j, k). For the *Pmp* rays traced with theoretical ray parameters, the reason for high ray density is twofold. First, the *Ss* ray density is higher at the corresponding virtual source locations (~980 and ~1580 km; Fig. 3i). Second, the *Ss* ray parameter changes from retrograde to prograde at these virtual source locations (~980 and ~2180 km; Fig. 3d), causing the ray parameter, hence incident angle at CMB, of *Pmp* rays to first increase than decrease, which produces additional focusing effects for the *Pmp* rays. For the *Pmp* rays traced with apparent ray parameters (Fig. 3k), only the second effect exists as the virtual sources are equally spaced in this case, which explains the weaker focusing effect. Due to the increased irregularity of the incident *Ss* wave front compared with the 1200 km-wavelength model in Fig. 2, the discrepancy between theoretical and apparent Φ_{VDSS} increases significantly (Fig. 3e). As a result, the discrepancy between the inferred and true V_p^{um} grows to ~4.5%. However, although significant lateral variation of lithospheric structure means that ray-theory approximations are insufficient to model Φ_{VDSS}, our back-projection method still recovers CMB depths reasonably well. Our back-projection image shows the Moho depth at 40±2 km along the

profile, close to the 40-km CMB depth in the original model (Figs. 3g, l). The Moho amplitude variation in our back-projection image (Figs. 3g, l) results from the uneven *Pmp* ray distribution. The amplitude is highest at ~1100 km where the CMB has the highest density of *Pmp* reflections points (Figs. 3j, k). As expected, the difference between the corrected and uncorrected Moho depth estimates grows due to the stronger lateral heterogeneity (Fig. 3l). We also tested stacking the back-projection images of two earthquakes, one from the west and one from the east, both with the same incident angle (35º; Figs. 3h, m). The resulting image gives an improved Moho depth estimation and smoother amplitude than given by a single earthquake (Figs. 3h, m).

Finally, we reduce the LAB wavelength to 400 km, and the average dip of the LAB becomes ~31º (Fig. 4a). The waveforms now show strong variation in *Ss* and *SsPmp* arrival time and amplitude (Figs. 4b, c). In addition to *Ss* and *SsPmp*, we observed additional seismic phases that can be fit by hyperbolae with H_0 = 200 km (largest LAB depth) and V = 4.61 km/s (lithospheric-mantle V_s; H1 in Fig. 4b) and H_0 = 40 km (CMB depth) and V = 6.5 km/s (crustal V_p; H2 in Fig. 4b). H1 shows opposite polarity on vertical and radial components, a polarization consistent with S wave, whereas H2 shows the same polarity on vertical and radial components, consistent with P wave (Figs. S1b, c). Combining the moveouts and polarizations of the two phases, we interpret H1 as a diffracted S wave generated by the incident S wave at the deepest points of the LAB, and H2 as a diffracted P wave generated by *SsPmp* at the CMB where *SsPmp* rays undergo multipathing (e.g. ~1100 km; Figs. 4i, j and Fig. S1a). The ray-tracing for *Ss* shows strong focusing atop the shallowest LAB from S rays traveling sub-parallel to the LAB (Fig. 4h). The strong LAB undulation also causes post-critical reflection at the LAB of a few S rays that meet the LAB with very high incident angles (Fig. 4h). These post-critically reflected S rays are widely dispersed at the surface (Fig. 4h) and have ray parameters higher than the reciprocal of crustal V_p (0.1538 s/km; Fig. 4d). This triplication behavior causes the *Ss* theoretical ray parameter to be multi-valued in the ranges 600-700 km, 1000-1100 km and 1400-1500 km. (Theoretical p_{Ss} at ~1500 km and ~1900 km is missing the high values at ~700 km and ~1100 km because the spacing of our initial *Ss* rays is not dense enough to capture the rapid variation of ray parameter at those two locations.) Apparent p_{Ss} generally agrees with theoretical p_{Ss}, except that apparent p_{Ss} lacks any abnormally high values. This is because apparent p_{Ss} derived from our synthetic waveforms only includes the first-arrival branch of the phase. Only very few of the rays with high p_{Ss} exist (Fig. 4h), causing them to have limited contribution to the *Ss* waveforms. The

results of P-ray tracing show a complicated pattern to the right of the shallowest part of the LAB (Figs. 4i, j). Due to the sharp peak of both apparent and theoretical *Ss* ray parameter vertically above the shallowest LAB (Fig. 4d), the take-off angles of down-going P rays first increase (retrograde branch) and then decrease with distance (prograde branch). The P rays of the two branches cross and cause focusing of *SsPmp* to the right of the shallowest LAB (e.g. ~1100 km; Figs. 4b, c, i, j), which in turn generates H2 (Fig. S1a). For cases with CMB topography discussed below, the VDSS ray parameter p_{VDSS} will be different from, and have more complex lateral variation than the *Ss* ray parameter. As a result of the strongly non-planar *Ss* at the free surface, theoretical Φ_{VDSS} is significantly different from apparent Φ_{VDSS} (Fig. 4e). Despite the complicated *Ss* and *SsPmp* waveforms, our back-projection method is still capable of imaging the CMB reasonably well, although the amplitude clearly varies along the Moho image (Figs. 4f, k). The only places where the discrepancy between the imaged Moho and the CMB exceeds 3 km are ~700-800 km, ~1100-1200 km and ~1500-1600 km, where the Moho depth estimates are deeper than the CMB (Figs. 4f, k). When comparing the corrected and uncorrected back-projection images in these ranges, we find that both images overestimate Moho depth, though the discrepancy in the corrected image is significantly smaller than the uncorrected one (Fig. 4k). Therefore, the error in our corrected back-projection image can be understood as insufficient correction for *Ss* travel-time variation. Including an earthquake from the opposite direction gives a smoother amplitude variation along the Moho image but yields little improvement in Moho depth estimate (Fig. 4l).

To test the effects of initial S-wave incident angles, we compute waveforms with incident angle of 33º and conducted back-projection with the synthetic data (Fig. S2). The image of the 33º earthquake (Figs. S2a, f) gives similar Moho depth estimations and shows similar amplitude variation as the 35º one (Figs. S2b, g) because the focusing and defocusing of *Pmp* rays happen at similar locations for both events. Due to the similarity between the 33º and 35º images, stacking them only yields limited improvement of the Moho depth estimation (Figs. S2c, h). Even including four earthquakes with both incident angles from both west and east only slightly improves the Moho depth estimation (Figs. S2e, j).

2.2. Effects of CMB Topography

In this section, we fix the LAB at 200 km-depth and model a sinusoidal CMB (Figs. 5, 6, 8). We fix the peaks and troughs of the CMB at 30 and 50 km-depth and vary the wavelength of the CMB between 1200, 600, and 400 km. The incident angle of the initial plane-S wave in the asthenosphere is fixed at p_0 = 35º, as in our previous models.

We first set the CMB wavelength to be 1200 km, in which the average dip of the CMB is ~2º (Fig. 5a). The synthetic waveforms aligned with apparent velocity $V_{app} = 1/p_0 = 7.84$ km/s shows a smooth sinusoidal change of *Ss* arrival time caused by the sinusoidal variation of CMB depth (Fig. 5b). Following the *Ss* arrival we observe clear *SsPmp* showing similar sinusoidal variation pattern but with a much larger range (Fig. 5b), that is, *SsPmp* arrival times are more sensitive to CMB variation than *Ss* arrival times (cf. Fig. 2). In addition to *Ss* and *SsPmp*, we observe another significant phase after *SsPmp* with similar travel-time variation but lower amplitude, likely *SsPmpPmp* (Fig. 5b). *SsPmpPmp* and other multiple P phases (e.g. $S_SPmsPmp$; Thompson et al., 2019; Yu et al., 2013) could in future be incorporated into back-projection or other imaging schemes. Due to lateral variation of CMB depth, the down-dip branches of *SsPmpPmp* are significantly amplified compared to the up-dip branch (Fig. 5b). We apply the same ray tracing scheme as before for *Ss* and observe negligible focusing effects, corresponding to minor change of *Ss* amplitude across the profile (Fig. 5h). As a result of the smooth variation of *Ss* arrival times, the theoretical and apparent *Ss* ray parameters are also quite close to p_0 = 0.1275 s/km (Fig. 5d), indicating relatively small deviation from a planar incident *Ss*. The *Pmp* rays traced with theoretical and apparent *Ss* ray parameters are almost identical, showing a near-uniform distribution of *Pmp* rays. However, despite the minor variation of *Ss* ray parameter, there are discrepancies of up to 60º between the theoretical and apparent Φ_{VDSS} (Fig. 5e). This discrepancy is likely caused by the non-planar CMB that makes *Pmp* deviate further from plane reflection waves. Specifically, the traced *Pmp* rays show pre-critical reflections (yellow rays in Figs. 5h, i) on the up-dip segment of the CMB and predict Φ_{VDSS} = 180º there, which is not observed in the apparent Φ_{VDSS} (Fig. 5e). We apply the same back-projection method described previously and observe that the imaged Moho agrees well with the CMB (±2 km; Figs. 5f, j), even though our back-projection scheme assumes horizontal reflectors, whereas the rays shown in Figs. 5h and i (also Figs. 6h, i, Figs. 8h, i, Figs. 9g, h, Figs. 10g, h, and Figs. S6g, h) are traced with the actual sinusoidal CMB geometry. Our corrected Moho depths are more consistent with

the true CMB compared with the uncorrected estimates because the correction accounts for the lateral variation of *Ss* ray parameter (hence ray parameter; Fig. 5j). The amplitude variation along the Moho is minor due to the near-uniform distribution of *Pmp* rays (Figs. 5i, j).

We next decrease the CMB wavelength to 600 km (average dip ~4º) and compute synthetic waveforms (Fig. 6a). The resulting *Ss* and *SsPmp* arrival times show sinusoidal variation with shorter wavelength (Figs. 6b, c), and the up-dip and down-dip branches of *SsPmpPmp* become more asymmetric (Fig. 6b) due to the increased dip on the CMB. The traced *Ss* rays are still relatively uniform (Fig. 6g), but the *Ss* ray parameter shows a stronger sinusoidal variation than the 1200-km-wavelength case (Fig. 6d). The ray tracing for *Pmp* shows significantly more uneven ray density and predicts pre-critical *SsPmp* on the up-dip segments of the CMB (Figs. 6e, h, i). Although the presence of pre-critical reflections is again not shown by apparent Φ_{VDSS} measurements (apparent Φ_{VDSS} is always < 180º; Fig. 6e), it has an effect on A_{VDSS}: the cyan trace has approximately the same amplitude as the blue one (Fig. 6k) despite having a higher incoming *Pmp* ray density (Figs. 6h, i) because the rays arriving at the cyan station are pre-critical and thus carry lower amplitude than the post-critical rays (Figs. 6h, i). This inconsistent manifestation of pre-critical reflections on Φ_{VDSS} and A_{VDSS} highlights the non-ray-theory behavior of the wavefield in this λ = 600 km case. Applying our back-projection scheme to the synthetic data yields a Moho image with higher amplitude at the CMB valleys and lower amplitude at the CMB ridges (Figs. 6f, j); the down-dip (up-dip) segments of the CMB are imaged at shallower (greater) depth (Figs. 6f, j). Two main factors contribute to the higher Moho amplitude at the CMB valleys than the CMB ridges. First, the traces back-projected to the CMB troughs have higher *SsPmp* amplitude (e.g. the green trace in Fig. 6k). Second, the CMB troughs have denser *SsPmp* reflection points (Figs. 6h, i). The same argument can explain the lower Moho amplitude at CMB peaks, where the *SsPmp* amplitude is low (e.g. the cyan trace in Fig. 6k) and the *SsPmp* reflection points are sparse (Figs. 6h, i). The discrepancies between the imaged Moho depth and true CMB depth for a dipping CMB raise the question whether the horizontal-reflector assumption in our back-projection scheme makes it unable to recover CMB dips precisely. Comparison of the corrected and uncorrected Moho depths shows that the uncorrected Moho depths show greater deviation from CMB depth, but with the same polarity (Fig. 6j). As before (Fig. 4k), this comparison implies that the discrepancy between the corrected Moho depths and the true CMB is likely due to insufficiently-corrected *Ss* travel time variation. By

including another earthquake with the same incident angle from the opposite direction, the CMB slopes are significantly better imaged (Figs. S3c, d) because the depth biases for the two events are opposite, thus offset each other in the stacked image.

To further investigate the ability of our back-projection method to recover CMB dip, we compute synthetic *SsPmp* waveforms using models with CMB ramps and apply our back-projection scheme to them (Fig. 7). To test the effects of CMB dip direction and dip angle, we generate models with ~±3º (CMB depth changing from 30 to 50 km across 400 km; positive indicates ray paths travelling in the down-dip direction; Figs. 7a, d) and ~±6º dip (CMB depth changing from 30 to 70 km across 400 km; Figs. 7g, j). The initial ray parameter and material properties are kept the same as previous examples. The vertical-component synthetic waveforms for the four earth models aligned on *Ss* arrival are shown in Figs. 7b, e, h, and k. We find that our back-projection method recovers the dipping angles of the CMB ramps well in all cases (Figs. 7c, f, i, l), except for local discrepancies with ramp dip of -6º (Fig. 7l). This discrepancy is likely due to strong multiples that locally interfere with *SsPmp* (Fig. 7k). These examples demonstrate that the horizontal-reflector assumption in our back-projection scheme is sufficient to image CMB with dip $\leq \pm 6º$. Since the CMB dip in Fig. 6 with a 600 km-wavelength CMB is < 6º, the discrepancies between our Moho image and the true CMB (Fig. 7j) are unlikely due to the horizontal-reflector assumption. Two factors may instead contribute to the discrepancy in our model with a 600 km-wavelength CMB and a flat LAB, and potentially all other models with sinusoidal CMB variation. First, the spatial variations of CMB depth in sinusoidal models are nonlinear, which might make it hard to image with our method. Second, the spatial range of ridge-to-valley CMB depth variation (300 km in Fig. 6, smaller than 400 km in Fig. 7) might be too small to be properly imaged with our method.

We finally decrease the CMB wavelength to 400 km (average dip ~6º; Fig. 8a) and compute synthetic waveforms. In addition to strong sinusoidal variation in *Ss* and *SsPmp* arrival times (Figs. 8b, c), *SsPmp* amplitude also varies dramatically (Figs. 8b, c, k). Due to high dip on the CMB, the up-dip branch of *SsPmp* is almost invisible, whereas the down-dip branch has strong amplitude (Fig. 8c). The ray tracing for *Ss* still shows relatively uniform ray distribution (Fig. 8g), in agreement with the small variation in *Ss* amplitude (Figs. 8b, c, k) and in contrast to *SsPmp*. As in the 600-km-CMB case, *SsPmp* amplitude is controlled by both *Pmp* ray density and energy carried by individual rays, as evidenced by the cyan trace having similar amplitude to

the blue one (Figs. 8k). The sharp changes in theoretical Φ_{VDSS} at ~900, ~1300 and ~1700 km (thick gray curve, Fig. 8e) are due to *Pmp* rays with a wide range of incident angle at the CMB arriving over a very narrow distance range (Figs. 8h, i). Our back-projection Moho image shows strong amplitude variation (Figs. 8f, j) due to the uneven distribution of *Pmp* rays (Figs. 8h, i) and strong variation of *SsPmp* amplitude (Figs. 8b, c, k). Although the corrected Moho depths (solid black curve in Fig. 8j) match the true CMB depths poorly in segments distant from the CMB valleys, they are still significantly better than the uncorrected Moho depths (dashed black curve in Fig. 8j). After including another earthquake from the opposite back azimuth, the CMB slopes are better resolved and the amplitude distribution becomes more even (Figs. S4b, d, g, i) as in the 600 km-CMB case. We again test the effects of including earthquakes with different incident angles. Surprisingly, the 33º event gives a poorer Moho image than the 35º event with artifacts near the CMB ridges (Figs. S4a, f) likely caused by locally weak *SsPmp* and strong *SsPmpPmp*. In this synthetic case, because the 33º event creates a poorer Moho image than the 35º event (Figs. S4a, b, f, g), including the 33º event in the stack actually decreases the image quality (Figs. S4a, c, f, h). With real data, the improvement in signal-to-noise ratio from stacking additional waveforms might outweigh the loss of image quality from including events with different incident angles.

2.3. Joint Effects of CMB and LAB Topography

Finally, we study earth models in which both the CMB and LAB show sinusoidal depth variation in order to test the ability of our back-projection method to image variations in CMB depth in the presence of LAB depth variation. Our models have the CMB and LAB assigned identical structural wavelength and are in-phase corresponding to frequent geologic observations, e.g. the CMB and LAB are both deep beneath collisional orogens and both shallow beneath rifts. We set depth ranges of the CMB and LAB at 30–50 km and 80–200 km, use the same material properties and initial S-wave incident angle as in the previous sections, and vary the structural wavelength between 1200, 600, and 400 km.

We first test our back-projection method on the model with a structure wavelength of 1200 km (Fig. 9a). The synthetic waveforms show very smooth variation of T_{VDSS}, and the *SsPmp* amplitude is almost constant across the profile (Figs. 9b, c, j). The multiple arrival is also visible following *SsPmp* (Fig. 9b and blue trace in Fig. 9j). The *Ss* ray parameter is very close to

the initial ray parameter p_0 = 0.1275 s/km across the profile, because the in-phase variation of thickness of the crust (low velocity) and lithospheric mantle (high velocity) counteracts each layer's individual effects on *Ss* arrival time, making *Ss* at the free surface closer to a plane wave. As expected, our back-projection procedure recovers the CMB geometry almost perfectly (±1 km; Figs. 9e, i).

As we decrease the structure wavelength to 600 km (Fig. 10a), the *Ss* and *SsPmp* arrival times show sinusoidal patterns with shorter wavelength (Figs. 10b, c). The variation of ray parameter (Fig. 10d) is less strong than for the case with flat LAB and 600 km-wavelength CMB (Fig. 6d) due to the in-phase variation of crustal and lithospheric thickness. Similarly, the back-projection image resolves the CMB well with slightly improved images of the CMB slopes (Figs. 10e, i) compared to the case with flat LAB and 600-km-wavelength CMB (Figs. 6f, j). As expected, the stack of earthquakes from both back azimuths further improves the Moho image (Figs. S5c, d). These results are encouraging because in-phase variation of CMB and LAB depth (Fig. 10a) may be more prevalent than a flat LAB beneath a variable CMB (Fig. 6a).

When the structure wavelength is reduced to 400 km (Fig. S6a), we observe absurdly complex waveforms resulting from both lateral variation in CMB and LAB that would likely defy confident interpretation on real data (Figs. S6b, c). The waveforms show complexities resulting from both undulating CMB (strong variation of *SsPmp* amplitude; Fig. S6j) and LAB (H1 and H2 as in Figs. 4b, c). This contrasts with the in-phase cancellation effects shown in the 1200 and 600 km-wavelength cases because at short wavelength the refraction points of the obliquely incident S rays at the CMB and LAB are at very different locations, preventing in-phase cancellation. Despite extremely complicated *SsPmp* waveforms and the generally low amplitude of *SsPmp* that makes it difficult to even discern on many traces (Figs. S6b, c, j), our back-projection method still yields correct Moho depths for the CMB valleys (Figs. S6e, i) due to the high *SsPmp* amplitude of traces reflected at those locations (e.g. green trace in Fig. S6j).

3. APPLICATION TO THE ORDOS BLOCK

The Ordos Block in northern China (Fig. 11b) is a site of considerable interest, as it is the surviving remnant of the Archean North China Craton (Liu et al., 1992). It is unknown why this region preserved its lithospheric root while the eastern part of the craton underwent significant modification (decratonization) during the Mesozoic (Gao et al., 2008; Menzies et al., 1993). The

crustal structure of the Ordos Block and the surrounding regions is expected to hold important clues for the evolution of the North China Craton and thus has been the subject of numerous previous studies. However, to date contradicting results have been reported regarding the crustal thickness of the Ordos Block. Studies using only receiver-function (RF) methods agree on a moderate crustal thickness of 40-45 km beneath most of the Ordos Block (Feng et al., 2017; Tian et al., 2011; Wang et al., 2014) [with the exception of He et al. (2018) who showed quite different RF images and inferred a thicker crust]. On the other hand, using VDSS, Yu et al. (2012) found that the crustal thickness close to the eastern margin of the Ordos Block is ~60 km, significantly larger than the values given by RF methods. Yu et al. (2012) interpreted the layer between 40 and 60 km depth as a mafic lower-crustal layer that has survived since the formation of the North China Craton. Because it has been recently recognized that lateral variation of lithospheric V_s can have significant effects on Moho depth retrieved from *SsPmp* observations (Part 1; Yu et al., 2016), and that strong lateral variation of LAB depth might be present below the eastern boundary of the Ordos Block (Chen et al., 2009; Guo et al., 2016), the VDSS Moho depth given by Yu et al. (2012) is likely affected by lateral heterogeneity in the lithospheric mantle. However, due to the 1D distribution of seismic stations in Yu et al. (2012) (gray triangles in Fig. 11b), it is rare to have an earthquake suitable for VDSS analysis in line with the recording array so that the effects of lateral variation in lithospheric structure can be quantified. The ChinArray, an ongoing project with the ultimate goal of covering China with a dense broadband seismic network, was active in northern China from 2016-2017, which enabled the simultaneous recording of a single event on stations that cover most of the Ordos Block and adjacent regions (Fig. 11). We use this dataset to demonstrate the application of our back-projection methods to real data and to remove the previously misleading effects of lateral variation in lithospheric structure on VDSS Moho depth.

Among all the events in the epicentral distance range of 40–60º recorded by the Ordos segment of the ChinArray, Event 2017-03-21, a M5.6 event with focal depth of 111.7 km (Fig. 11a) was recorded by the most stations (Fig. 11b) and had a short source time function (Fig. 12d) that facilitates further analysis. We first filtered all the traces of this event between 0.05–0.5 Hz and used the Crazyseismic software package (Yu et al., 2017) to manually pick the records with clear *Ss* and *SsPmp* arrivals. We then separated the picked traces into pseudo-P and pseudo-S components using a particle-motion analysis algorithm (Yu et al., 2013). We assume that the

separated S-component records only contain *Ss* arrivals and used multicomponent cross correlation to align them, yielding the *Ss* travel time residuals with respect to the AK135 earth model (Kennett et al., 1995) at the recording stations (Fig. 11b). We stacked the pseudo-S-component seismograms to estimate the source time function and shift all the traces so that the positive peak on the source time function is at time zero. This process guarantees the correct reference value for measuring T_{VDSS}. On our travel-time-residual map, we observe a clear clustering of negative residuals (early arrivals) in the northern Ordos Block and positive residuals (late arrivals) in the Weihe Graben and Shanxi Graben (Fig. 11b). The negative residuals cluster in the northern Ordos Block, not the center, because the seismic rays come from the south and project the footprint of the thick and fast lithospheric root beneath central Ordos Block to the north of it. We then choose one of the trajectories from the event that traverses the most stations and project the stations within 30 km away from the trajectory to it in order to form a 1D linear array (Fig. 11b). The profile does not extend northward beyond ~39º because the records in that region suffer severely from multiples generated by the low-velocity sedimentary layer that covers most of the northern Ordos Block (Wang et al., 2014). Because our event is from similar back azimuth and epicentral distance as the events used in Yu et al. (2012) (Fig. 11a) our profile crosses the area where Yu et al. (2012) found overthickened crust (black oval in Fig. 11b), offering a chance for direct comparison between the two studies. The northward decrease of *Ss* travel-time residuals (Figs. 11b, 12b) highlights the need to account for lateral variation in lithospheric structure. In order to make travel-time residuals and ray parameters smooth functions of distance, we use a third-degree polynomial to fit the residuals (Fig. 12b). We then take the spatial derivative of the travel-time residuals and add it to the ray parameters predicted by the AK135 model to derive the observed ray parameter (Fig. 12c), which has a significantly wider variation than the predicted ray parameter (Fig. 12c). The wide range of observed ray parameter also corresponds to a wide range of turning velocity, from ~7.2 km/s in the south to ~8.4 km/s in the north (Fig. 12c).

We observe similar clear *Ss* arrivals on the pseudo-S-component seismograms across different stations. On the pseudo-P-component seismograms, T_{VDSS} increases significantly northward from the Weihe Graben (~5s) to the central Ordos Block (~10s). Using Eqn. 1 with an average crustal V_p = 6.2 km/s and ray parameter p = 0.13 s/km, the observed variation in T_{VDSS} corresponds to a change of crustal thickness from ~26 km beneath the Weihe Graben to ~52 km

beneath the central Ordos Block, significantly greater than the variation shown by RF methods (30-45 km; Figs. 12g, h) (Feng et al., 2017; Wang et al., 2014). The apparent greater variation in VDSS Moho depth results from lateral variation of both *Ss* travel-time residual and ray parameter (Figs. 12b, c). To properly address this problem, we apply our back-projection method (section 2.1.2) to the pseudo-P-component seismograms. First, we measure Φ_{VDSS} on each trace along the profile (diamonds in Fig. 12f) and find a clear decreasing trend. This observation is important because by contrast a flat CMB would cause increasing Φ_{VDSS} with decreasing ray parameter along the profile (Part 1). Two factors may cause the decrease of Φ_{VDSS} with distance. First, as will be shown later, the CMB deepens northward along the profile, a situation modelled in our synthetic with 600 km-wavelength CMB and flat LAB, where Φ_{VDSS} decreases from ~160º to ~30º as range increases from ~1100–1300 km (Figs. 6a, e). Second, because the sedimentary layer above the Ordos Block becomes thicker and probably slower northward along our profile (Wang et al., 2014) the sedimentary layer has stronger effects on *SsPmp* waveforms in the north than in the south, which might manifest itself as a decrease in observed Φ_{VDSS}. Before applying our phase-shift correction, we discarded two measurements of Φ_{VDSS} = 180º that are apparently erroneous (gray diamonds in Fig. 12f) and interpolated Φ_{VDSS} as a function of distance using a second-degree polynomial (red curve in Fig. 12f). Since the *Ss* arrivals are aligned by their positive peaks, we used the fitted Φ_{VDSS} as a function of distance to correct the phase shift of each pseudo-P-component trace to 0º, so that T_{VDSS} of each trace is at the positive peak. To address uneven station distribution in this real dataset, we interpolated the pseudo-P-component traces to 10 km bins. We then used V_p^{av} = 6.2 km/s (including sedimentary layers, Xia et al., 2017), to back project the phase-shift-corrected and interpolated pseudo-P-component traces. Our data-processing work flow, from wave-mode separation to back projection, is summarized in Fig. 13. We picked the Moho depths at the maximum positive amplitude for each location because the phase shift of each input trace was corrected to 0º. We compute two back-projection images, one with zero travel-time residual and the AK135-predicted ray parameter ("uncorrected"; Moho-depth picks are shown with black dotted curves in Figs. 12g and h), and one using the observed travel-time residual and ray parameter ("corrected"; Fig. 12h; Moho-depth picks are shown with black solid curves in Fig. 13h), so that the effects of lateral variation in lithospheric structure can be identified. For comparison, we project the RF Moho depths given by Feng et al. (2017) on stations within 30 km to our profile and plot them on the two back-

projection images (yellow circles in Figs. 12g, h). We also plot the approximate depth of the bottom of the "growth zone" in the range where the layer is identified in He et al. (2018) (yellow dotted lines in Figs. 12g, h). Because our back-projection requires known p_{Ss} at the virtual source and the receiver, our back-projection image only gives reliable results in the range 180-450 km (hereafter the profile), which includes the transition from the Weihe Graben to the Ordos Block (Figs. 12g, h). On the uncorrected image, the Moho starts at ~35 km-depth beneath the Weihe Graben and gradually deepens northward, reaching ~56 km-depth in the central Ordos Block (Fig. 12g), ~15 km deeper than the RF Moho from Feng et al. (2017), though the RF Moho shows strong variability (Fig. 12g) perhaps due to W-E variation and effects of sedimentary layer. This discrepancy between our uncorrected VDSS and RF Moho is similar to that shown by Yu et al. (2012) and interpreted as overthickened crust (gray diamond in Fig. 12g), as should be expected because neither our uncorrected Moho image nor Yu et al. (2012) accounts for lateral variation in lithospheric structure. In contrast, on our corrected image, the VDSS Moho depth is consistent with RF Moho from 180-250 km (Fig. 12h), then gradually deepens northward to ~50 km at the northern end of the profile. Our VDSS Moho becomes significantly flatter (less steep) after correction because the effects of *Ss* travel time variation is removed (Fig. 12h). The discrepancy between VDSS Moho and RF Moho from Feng et al., (2017) decreases significantly after correction, though the corrected VDSS Moho is still deeper beneath the central Ordos Block (Fig. 12h). On the other hand, the bottom of the "growth zone" from He et al. (2018) appears to agree well with the corrected VDSS Moho beneath the central Ordos Block (Fig. 12h), whereas the uncorrected VDSS Moho is significantly deeper (Fig. 12h). In summary, the above example with real data shows that our back-projection method using observed travel-time residuals and ray parameters improves VDSS Moho depth estimates in regions with significant lateral variation in lithospheric structure.

We conduct additional tests to explore possible reasons for the discrepancy between our corrected VDSS Moho depth and the RF Moho depth from Feng et al. (2017). Fig. 14b shows the corrected VDSS Moho computed with V_p^{av} = 6.0 km/s (gray dotted curve in Fig. 14b), which is significantly shallower than that calculated with average crustal V_p^{av} = 6.2 km/s and in better agreement with the Feng et al. (2017) RF Moho in the segment beyond 300 km (Fig. 15d). Since the sedimentary layer in the Ordos Plateau thickens towards the interior of the plateau (Yang et al., 2005), the northern part of our profile might indeed have a lower V_p^{av} than the southern part.

Our observed decrease of Φ_{VDSS} with distance (Fig. 12f) appears to conflict with the decrease of ray parameter with distance (Fig. 12c), raising the possibility that observed Φ_{VDSS} might be inaccurate, in which case our phase-shift correction would be wrong. To test this hypothesis, we apply a -90º-phase-shift correction to all pseudo-P-component traces, which is equivalent to assuming all traces have Φ_{VDSS} = 90º. We chose 90º because the traces with highest A_{VDSS}, thus likely most accurate Φ_{VDSS} measurements have Φ_{VDSS} = ~90º at ~250 km (Fig. 12f). Applying our back-projection method to these phase-shift-corrected traces with V_p^{av} = 6.2 km/s, we produce an image with significantly flatter Moho and better agreement with RF Moho depths from Feng et al. (2017) (solid gray curve in Figs. 14c, d). Nonetheless, this better agreement does not necessarily indicate that the -90º-phase-shift correction is superior to the correction method using variable Φ_{VDSS} because as will be discussed later, the RF Moho depths themselves might be unreliable. The main goal for this test with -90º-phase-shift correction is to quantify the potential uncertainties (up to 10 km; Fig. 14d) that could be caused by inappropriately correcting for phase shifts in our back-projection process.

We identify four additional possible reasons for the discrepancy between our corrected VDSS Moho and the RF Moho from Feng et al. (2017). First, we have shown with our synthetic tests that our back-projection method might be insufficient to correct the effects of *Ss* travel time variation, particularly when lateral heterogeneity is strong (i.e. Figs. 4 and 98). In our Ordos case, although the crust thickens northward along the profile (Figs. 12g, h), the dramatic northward decrease of *Ss* travel-time residual indicates that the northward thickening of lithosphere (deepening of the LAB) has the dominant effect (Fig. 12b). In our synthetic cases where LAB depth changes dominate *Ss* travel-time variation (e.g. Figs. 3, 4), and the deepening LAB causes an increased Moho depth in the uncorrected back-projection image (e.g. 1100-1300 km in Fig. 4k), the corrected Moho depth also remains slightly deeper than the true CMB depth. In our synthetic example with 400 km-wavelength LAB and flat CMB, the range of *Ss* travel-time residuals is ~1s, and the remnant discrepancy between the corrected VDSS Moho depth and true CMB depth is ~2 km (Fig 4k). Because in our Ordos case the range of *Ss* travel time residual is ~2.5 s, simple scaling suggests a remnant discrepancy between our corrected VDSS Moho depth and true CMB depth of ~5 km, which could explain most of the discrepancy between our VDSS Moho and the Feng et al. (2017) RF Moho (Fig. 12h). Second, our VDSS Moho might not represent the true CMB in this region. Because the *SsPmp* turning velocity is > 8.33 km/s for

most of the range beyond 250 km (Fig. 12c), higher than the *Pn* velocity given by active-source studies in this region (~8.3 km/s) (Jia et al., 2014), *SsPmp* waves might become refractions in the upper mantle due to their high turning velocity. This phenomenon would cause an apparently deeper VDSS Moho because the upper mantle above the *SsPmp* turning depth would also be included in the crustal depth estimation (for more discussion on this possibility see Part 2). Third, the Moho found by Feng et al. (2017) may not represent the true CMB in this region. As shown in He et al. (2018), a "growth zone" with V_p = 6.2–7.5 km/s extending down to ~50 km might exist beneath north-central Ordos Plateau (yellow dashed line in Fig. 12g, h). If this interpretation is true, our VDSS Moho will represent the true CMB, whereas Feng et al. (2017) might have identified an intra-crustal interface, possibly the top of the "growth zone", as the CMB. Finally, published RF Moho depths typically ignore significant heuristic uncertainty in the choices of V_p^{av} and multiple stacking weights, again allowing the possibility that our VDSS Moho marks the true CMB and the RF Moho is in error.

4. CONCLUSIONS

Post-critical *SsPmp* has three major attributes: T_{VDSS}, Φ_{VDSS} and A_{VDSS}. An outstanding question about *SsPmp* waveforms in 2D is to what extent these attributes can be modeled with ray theory. With our synthetic examples, we show that variation of A_{VDSS} can be qualitatively explained with *SsPmp* ray density, and with amplitude-with-angle variation that largely depends on whether the ray underwent pre-critical or post-critical reflection at the CMB. In this paper we only model undulating CMB and LAB. In field observations the effects of CMB and LAB variability on A_{VDSS} are usually combined with the effects of sedimentary layers and can only be distinguished using array data and/or prior knowledge of sedimentary-basin geometry. Modeling Φ_{VDSS} with ray theory is largely unsuccessful except in cases with very smoothly varying LAB topography ($\lambda > 1200$ km) because ray-theory predictions of Φ_{VDSS} implicitly assume a planar down-going P wave incident at the CMB, which is invalid when *Ss* at the free surface is significantly non-planar (e.g. Figs. 3 and 4). In addition, a curved CMB further distorts the *SsPmp* wave front from the assumed plane-reflected wave (e.g. Fig. 5). Therefore, inferring V_p^{um} from Φ_{VDSS} in the presence of significant lateral heterogeneity requires methods to properly model non-planar-wave behavior of *SsPmp* without the need for expensive numeric simulations.

A possible solution is to use Kirchhoff Theory to model a curved wave front and its interaction with curved interfaces (Shearer, 1999), which is a direction for future research.

In contrast to A_{VDSS} and Φ_{VDSS}, T_{VDSS} can be quantitatively modeled with ray theory in a heterogeneous lithosphere, as evidenced by the success of our back-projection method. Our synthetic tests show that in most cases where *SsPmp* can be reliably observed (with strong amplitude), our back-projection procedure is capable of imaging the CMB reasonably well. On the other hand, when *SsPmp* amplitude is abnormally low (e.g. Fig. S5), a closer inspection of the data is required before inferring Moho depth. In general, we find *SsPmp* amplitude a useful diagnostic for the reliability of back-projection images. Other seismic methods that use reverberations of teleseismic body waves to image the Earth's deep structure (e.g. Shearer and Buehler, 2019) likely face similar problems as VDSS. Therefore, our back-projection method may have broader application in global seismology.

Acknowledgements:

Tianze Liu is supported by a Stanford Graduate Fellowship. We thank Steve Roecker and Greg Beroza for their valuable suggestions. Synthetics were calculated using SPECFEM2D, generously made available by Dimitri Komatitsch, who provided much guidance before his recent death.

References:

Aki, K., Richards, P.G., 2002. Reflection and transmission of P-SV across a solid-solid interface, in: Ellis, J. (Ed.), Quantitative Seismology (2nd Edition). University Science Books, pp. 139–145.

Buehler, J.S., Shearer, P.M., 2017. Uppermost mantle seismic velocity structure beneath USArray. J. Geophys. Res. 122, 436–448. doi:10.1002/2016JB013265

Chen, L., Cheng, C., Wei, Z., 2009. Seismic evidence for significant lateral variations in lithospheric thickness beneath the central and western North China Craton. Earth Planet. Sci. Lett. 286, 171–183. doi:10.1016/j.epsl.2009.06.022

Feng, M., An, M., Dong, S., 2017. Tectonic history of the Ordos Block and Qinling Orogen inferred from crustal thickness. Geophys. J. Int. 210, 303–320. doi:10.1093/gji/ggx163

Fischer, K.M., Ford, H.A., Abt, D.L., Rychert, C.A., 2010. The Lithosphere-Asthenosphere Boundary. Annu. Rev. Earth Planet. Sci. 38, 551–575. doi:10.1146/annurev-earth-040809-152438

Fliedner, M.M., Ruppert, S., Southern Sierra Nevada Continental Dynamic Working Group, 1996. Three-dimensional crustal structure of the southern Sierra Nevada from seismic fan profiles and gravity modeling. Geology 24, 367–370.

Gao, S., Rudnick, R.L., Xu, W.L., Yuan, H.L., Liu, Y.S., Walker, R.J., Puchtel, I.S., Liu, X., Huang, H., Wang, X.R., Yang, J., 2008. Recycling deep cratonic lithosphere and generation of intraplate magmatism in the North China Craton. Earth Planet. Sci. Lett. 270, 41–53. doi:10.1016/j.epsl.2008.03.008

Guo, Z., Afonso, J.C., Qashqai, M.T., Yang, Y., Chen, Y.J., 2016. Thermochemical structure of the North China Craton from multi-observable probabilistic inversion: Extent and causes of cratonic lithosphere modification. Gondwana Res. 37, 252–265. doi:10.1016/j.gr.2016.07.002

He, Y., Zheng, T., Ai, Y., Hou, G., Chen, Q.F., 2018. Growth of the lower continental crust via the relamination of arc magma. Tectonophysics 724–725, 42–50. doi:10.1016/j.tecto.2018.01.006

Hopper, E., Fischer, K.M., 2018. The Changing Face of the Lithosphere-Asthenosphere Boundary: Imaging Continental Scale Patterns in Upper Mantle Structure Across the Contiguous U.S. With Sp Converted Waves. Geochemistry, Geophys. Geosystems 19, 2593–2614. doi:10.1029/2018GC007476

Jia, S., Wang, F., Tian, X., Duan, Y., Zhang, J., Liu, B., Lin, J., 2014. Crustal structure and tectonic study of North China Craton from a long deep seismic sounding profile. Tectonophysics 627, 48–56. doi:10.1016/j.tecto.2014.04.013

Kang, D., Yu, C., Ning, J., Chen, W., 2016. Simultaneous Determination of Crustal Thickness and *P* Wavespeed by Virtual Deep Seismic Sounding (VDSS). Seismol. Res. Lett. 87, 1104–1111. doi:10.1785/0220160056

Kennett, B.L.N., Engdahl, E.R., Buland, R., 1995. Constraints on seismic velocities in the Earth from traveltimes. Geophys. J. Int. 122, 108–124. doi:10.1111/j.1365-246X.1995.tb03540.x

Klemperer, S.L., Hauge, T.A., H, E.C., Oliver, J.E., Potter, C.J., 1986. The Moho in the northern Basin and Range province, Nevada, along the COCORP 40{degrees}N seismic-reflection

transect. Geol. Soc. Am. Bull. 97, 603–618. doi:10.1130/0016-7606(1986)97

Komatitsch, D., Martin, R., Tromp, J., Taylor, M.A., Wingate, B.A., 2001. Wave propagation in 2-D elastic media using a spectral element method with triangles and quadrangles. J. Comput. Acoust. 9, 703–718. doi:10.1142/S0218396X01000796

Komatitsch, D., Vilotte, J.-P., 1998. The Spectral Element Method : An Efficient Tool to Simulate the Seismic Response of 2D and 3D Geological Structures. Bull. Seismol. Soc. Am. 88, 368–392.

Liu, D.Y., Nutman, A.P., Compston, W., Wu, J.S., Shen, Q.H., 1992. Remnants of ≥3800 Ma crust in the Chinese part of the Sino-Korean craton. Geology 20, 339–342. doi:10.1130/0091-7613(1992)020<0339:romcit>2.3.co;2

Liu, T., Klemperer, S.L., Yu, C., Ning, J., 2018. Post-critical SsPmp and its applications to Virtual Deep Seismic Sounding (VDSS)—1: sensitivity to lithospheric 1-D and 2-D structure. Geophys. J. Int. 215, 880–894. doi:10.1093/gji/ggy307

Liu, T., Klemperer, S.L., Ferragut, G., Yu, C., 2019. Post-critical SsPmp and its applications to Virtual Deep Seismic Sounding (VDSS) – 2: 1-D imaging of the crust/mantle and joint constraints with receiver functions. Geophys. J. Int. 219, 1334–1347. doi:10.1093/gji/ggz370

Luo, S., Zhu, L., Huang, R., Luo, Y., Jiang, X., Hua, Y., 2018. Determination of crustal thickness and velocities by using receiver functions and PmP travel times. Geophys. J. Int. 216, 1304–1312. doi:10.1093/gji/ggy500

Menzies, M.A., Fan, W., Zhang, M., 1993. Palaeozoic and Cenozoic lithoprobes and the loss of >120 km of Archaean lithosphere, Sino-Korean craton, China. Geol. Soc. London, Spec. Publ. 76, 71–81. doi:10.1144/GSL.SP.1993.076.01.04

Parker, E.H., Hawman, R.B., Fischer, K.M., Wagner, L.S., 2016. Estimating crustal thickness using SsPmp in regions covered by low-velocity sediments: Imaging the Moho beneath the Southeastern Suture of the Appalachian Margin Experiment (SESAME) array, SE Atlantic Coastal Plain. Geophys. Res. Lett. 43, 9627–9635. doi:10.1002/2016GL070103

Shearer, P.M., 1999. Kirchoff Theory, in: Introduction to Seismology. pp. 133–138.

Shearer, P.M., Buehler, J., 2019. Imaging Upper-Mantle Structure Under USArray Using Long-Period Reflection Seismology. J. Geophys. Res. 1–15. doi:10.1029/2019jb017326

Thompson, D.A., Rawlinson, N., Tkalčić, H., 2019. Testing the limits of virtual deep seismic

sounding via new crustal thickness estimates of the Australian continent. Geophys. J. Int. 787–800. doi:10.1093/gji/ggz191

Tian, X., Chen, Y., Tseng, T.L., Klemperer, S.L., Thybo, H., Liu, Z., Xu, T., Liang, X., Bai, Z., Zhang, X., Si, S., Sun, C., Lan, H., Wang, E., Teng, J., 2015. Weakly coupled lithospheric extension in southern Tibet. Earth Planet. Sci. Lett. 430, 171–177. doi:10.1016/j.epsl.2015.08.025

Tian, X., Teng, J., Zhang, H., Zhang, Z., Zhang, Y., Yang, H., Zhang, K., 2011. Structure of crust and upper mantle beneath the Ordos Block and the Yinshan Mountains revealed by receiver function analysis. Phys. Earth Planet. Inter. 184, 186–193. doi:10.1016/j.pepi.2010.11.007

Tromp, J., Komatitsch, D., Liu, Q., 2008. Spectral-element and adjoint methods in seismology. Commun. Comput. Phys. 3, 1–32.

Tseng, T.L., Chen, W.P., Nowack, R.L., 2009. Northward thinning of Tibetan crust revealed by virtual seismic profiles. Geophys. Res. Lett. 36, 1–5. doi:10.1029/2009GL040457

Wang, C.Y., Sandvol, E., Zhu, L., Lou, H., Yao, Z., Luo, X., 2014. Lateral variation of crustal structure in the Ordos block and surrounding regions, North China, and its tectonic implications. Earth Planet. Sci. Lett. 387, 198–211. doi:10.1016/j.epsl.2013.11.033

Xia, B., Thybo, H., Artemieva, I.M., 2017. Seismic crustal structure of the North China Craton and surrounding area: Synthesis and analysis. J. Geophys. Res. Solid Earth 5181–5207. doi:10.1002/2016JB013848

Yang, Y., Li, W., Ma, L., 2005. Tectonic and stratigraphic controls of hydrocarbon systems in the Ordos basin: A multicycle cratonic basin in central China. Am. Assoc. Pet. Geol. Bull. 89, 255–269. doi:10.1360/10070404027

Yu, C., Chen, W.P., van der Hilst, R.D., 2016. Constraints on residual topography and crustal properties in the western United States from virtual deep seismic sounding. J. Geophys. Res. Solid Earth 121, 5917–5930. doi:10.1002/2016JB013046

Yu, C., Zheng, Y., Shang, X., 2017. Crazyseismic: A MATLAB GUI-based software package for passive seismic data preprocessing. Seismol. Res. Lett. 88, 410–415. doi:10.1785/0220160207

Yu, C.Q., Chen, W.P., Ning, J.Y., Tao, K., Tseng, T.L., Fang, X.D., John Chen, Y., van der Hilst, R.D., 2012. Thick crust beneath the Ordos plateau: Implications for instability of the

North China craton. Earth Planet. Sci. Lett. 357–358, 366–375. doi:10.1016/j.epsl.2012.09.027

Yu, C.Q., Chen, W.P., van der Hilst, R.D., 2013. Removing source-side scattering for virtual deep seismic sounding (VDSS). Geophys. J. Int. 195, 1932–1941. doi:10.1093/gji/ggt359

Yu, C., Chen, W.P., van der Hilst, R.D., 2016. Constraints on residual topography and crustal properties in the western United States from virtual deep seismic sounding. J. Geophys. Res. Solid Earth 121, 5917–5930. doi:10.1002/2016JB013046

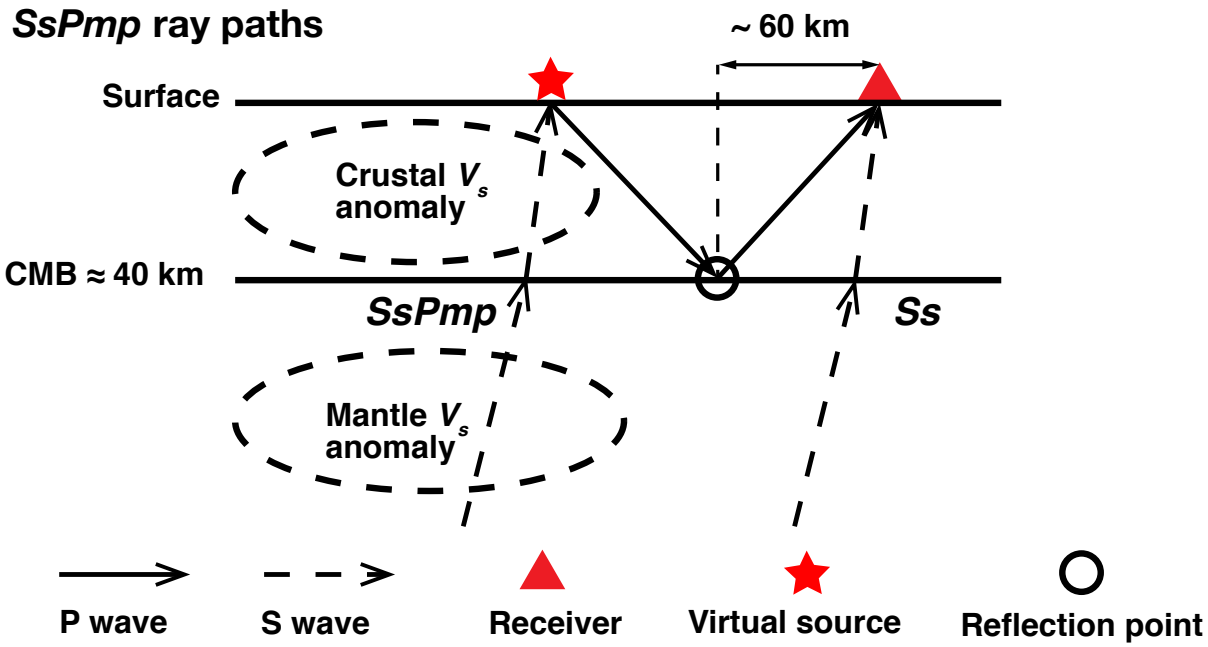

Figure 1. Ray paths of post-critical *SsPmp*. Note the large separation (> 100 km) between virtual source and receiver, making *SsPmp* sensitive to lateral heterogeneity in the crust and mantle lithosphere. CMB: crust-mantle boundary.

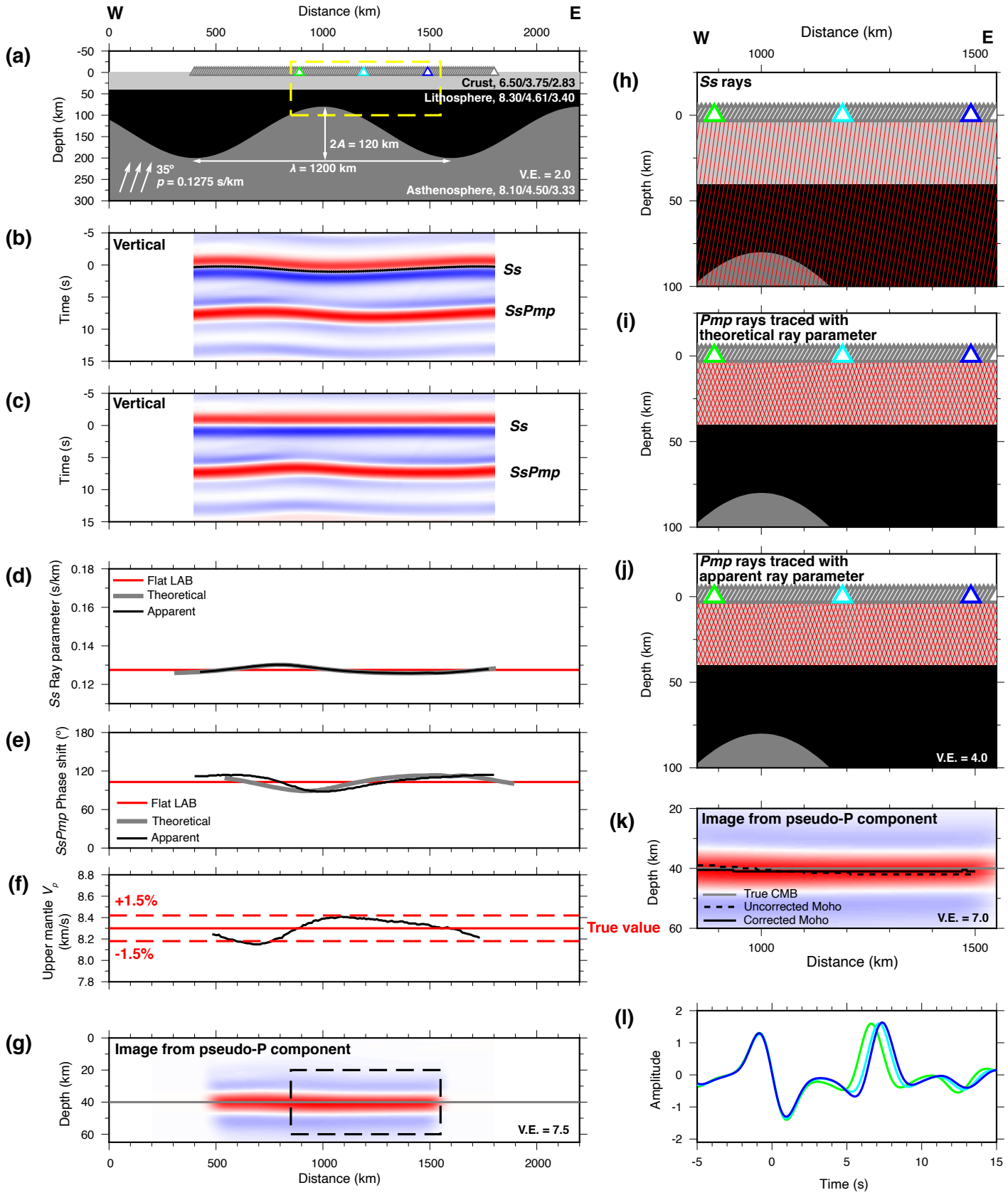
(a)
W
Distance (km)
E
Depth (km)
Crust, 6.50/3.75/2.83
Lithosphere, 8.30/4.61/3.40
2A = 120 km
λ = 1200 km
35°
p = 0.1275 s/km
V.E. = 2.0
Asthenosphere, 8.10/4.50/3.33
(b)
Vertical
Time (s)
Ss
SsPmp
(c)
Vertical
Time (s)
Ss
SsPmp
(d)
Ss Ray parameter (s/km)
Flat LAB
Theoretical
Apparent
(e)
SsPmp Phase shift (°)
Flat LAB
Theoretical
Apparent
(f)
Upper mantle Vp (km/s)
+1.5%
-1.5%
True value
(g)
Image from pseudo-P component
Depth (km)
V.E. = 7.5
Distance (km)
(h)
W
Distance (km)
E
Ss rays
Depth (km)
(i)
Pmp rays traced with theoretical ray parameter
Depth (km)
(j)
Pmp rays traced with apparent ray parameter
Depth (km)
V.E. = 4.0
(k)
Image from pseudo-P component
Depth (km)
True CMB
Uncorrected Moho
Corrected Moho
V.E. = 7.0
Distance (km)
(l)
Amplitude
Time (s)

Figure 2. Synthetic test using a sinusoidal LAB with horizontal wavelength of 1200 km, and peak and trough at 80 and 200 km-depth respectively, i.e. $2A/\lambda = 0.1$, $\theta_{av} \sim 11^{\circ}$. The CMB is flat at 40 km depth. (a) Model setup (vertical exaggeration x2): crust (light gray), lithosphere (black) and asthenosphere (dark gray) are labeled with their V_p/V_s/density. Triangles are 10 km-spaced seismic stations; green, cyan and blue edges identify stations recording the green, cyan and blue waveforms in (l). Arrows: incident angle of the plane S wave at the bottom of the model, with the same x2 vertical exaggeration. Yellow dashed box is area of model enlarged in (h), (i) and (j). (b) Vertical-component synthetic waveforms recorded at each station and aligned to the theoretical S arrival times for a constant ray parameter p_{Ss} of 0.1275 s/km. Continuous line of black dots: observed S arrival time residuals derived with multi-channel cross-correlation. (c) Same as (b), except that the waveforms are aligned to the observed S arrival times. (d) p_{Ss} calculated either by ray tracing (theoretical; thick gray curve) or by differentiating S arrival time with respect to horizontal distance (apparent; thin black curve). The p_{Ss} applicable to any *SsPmp* observation is measured at the virtual source point, so is plotted at the trace location where p_{Ss} is measured. Apparent p_{Ss} can only be measured from an actual recording so is not plotted west of the western trace at km 850 in (b). Red line: p_{Ss} = 0.1275 s/km, i.e. for model parameters as shown but with flat LAB. (e) *SsPmp* phase shifts relative to direct *Ss* (Φ_{VDSS}) either computed for each traced *SsPmp* ray assuming plane incident wave (theoretical; gray curve) or measured from P-component synthetic waveforms (apparent; black curve). Red line: Φ_{VDSS} for model parameters as shown but with a flat LAB. (f) Black curve: upper-mantle V_p^{um} measured from apparent Φ_{VDSS} assuming a plane wave incident at the CMB and plotted at the *Pmp* reflection point. Red solid line: true V_p^{um} = 8.30 km/s. Red dashed lines: ± 1.5% perturbation from the true V_p^{um}. (g) Back-projection image of the pseudo-P -component synthetic data corrected to 90º phase shift (vertical exaggeration x7.5). Gray line: true CMB depth. Black dashed box is area enlarged in (k). (h) Enlargement of yellow box in (a) with traced S rays plotted in red. (i) The same as (h), except plotting *Pmp* rays traced with the theoretical *Ss* ray parameters (thick gray curve in (d)). (j) The same as (i), except plotting *Pmp* rays traced with apparent *Ss* ray parameters (thin. black curve in (d)). (k) Enlargement of black dashed box in (g). Black solid curve: the maximum amplitude at each horizontal location picked as the observed Moho depth. Black dashed curve: observed Moho depths from back-projection images assuming a constant ray parameter (0.1275 s/km) and zero travel-time residual (equivalent to assuming a 1D earth model). (l) waveforms recorded at the green, cyan and blue stations in (a), colored accordingly.

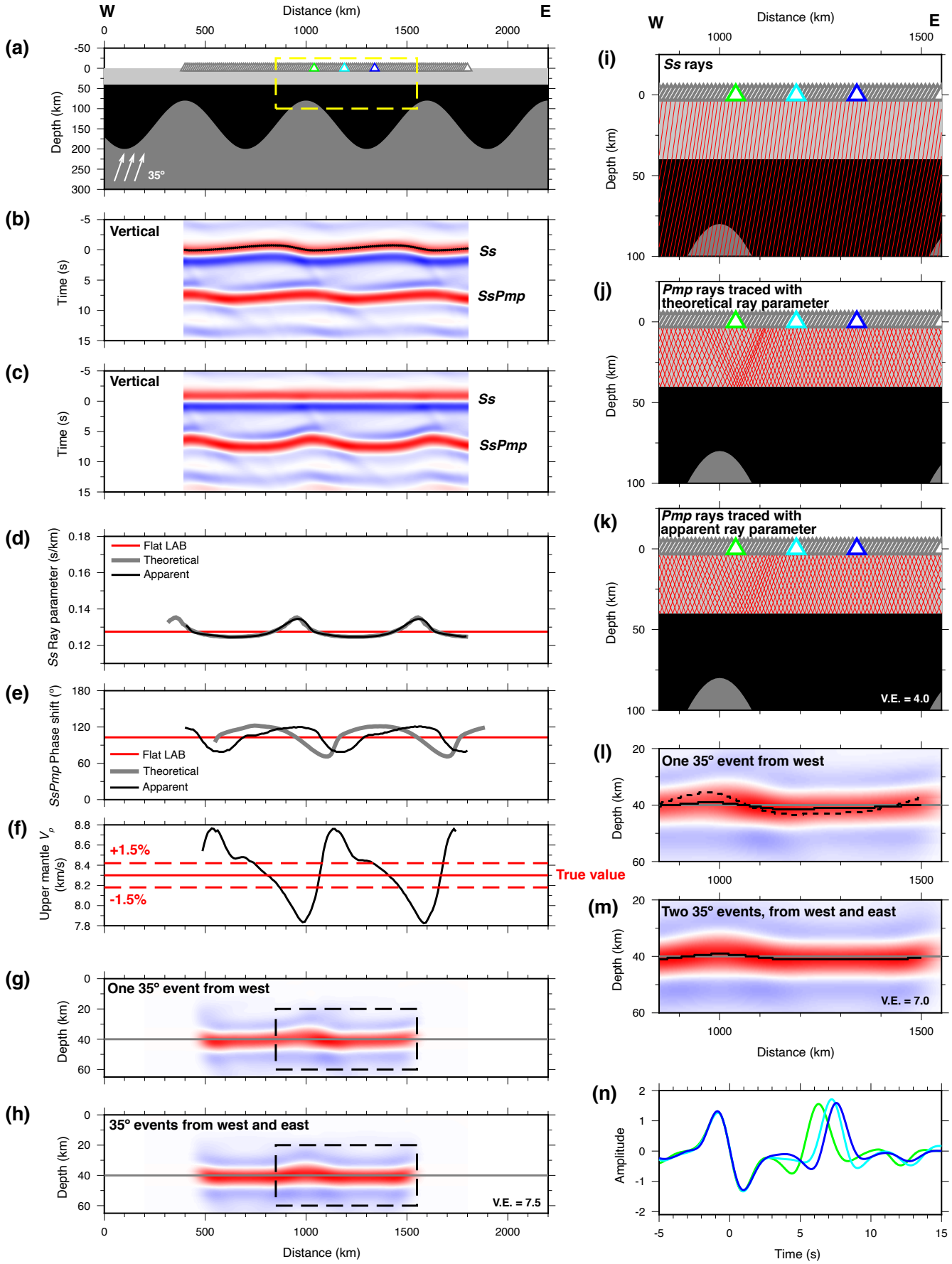
(a)
W
Distance (km)
E
Depth (km)
35°
(b)
Vertical
Ss
SsPmp
Time (s)
(c)
Vertical
Ss
SsPmp
Time (s)
(d)
Ss Ray parameter (s/km)
Flat LAB
Theoretical
Apparent
(e)
SsPmp Phase shift (°)
Flat LAB
Theoretical
Apparent
(f)
Upper mantle V_p (km/s)
+1.5%
-1.5%
True value
(g)
One 35° event from west
Depth (km)
(h)
35° events from west and east
V.E. = 7.5
Depth (km)
Distance (km)
(i)
Ss rays
Depth (km)
(j)
Pmp rays traced with theoretical ray parameter
Depth (km)
(k)
Pmp rays traced with apparent ray parameter
V.E. = 4.0
Depth (km)
(l)
One 35° event from west
Depth (km)
(m)
Two 35° events, from west and east
V.E. = 7.0
Depth (km)
Distance (km)
(n)
Amplitude
Time (s)

Figure 3. As Fig. 2, now computed with a 600 km-wavelength LAB (θ_{av} ~ 22º). (h) and (m) are stacked back-projection images of two events with the same incident angle (35º) coming from west and east.

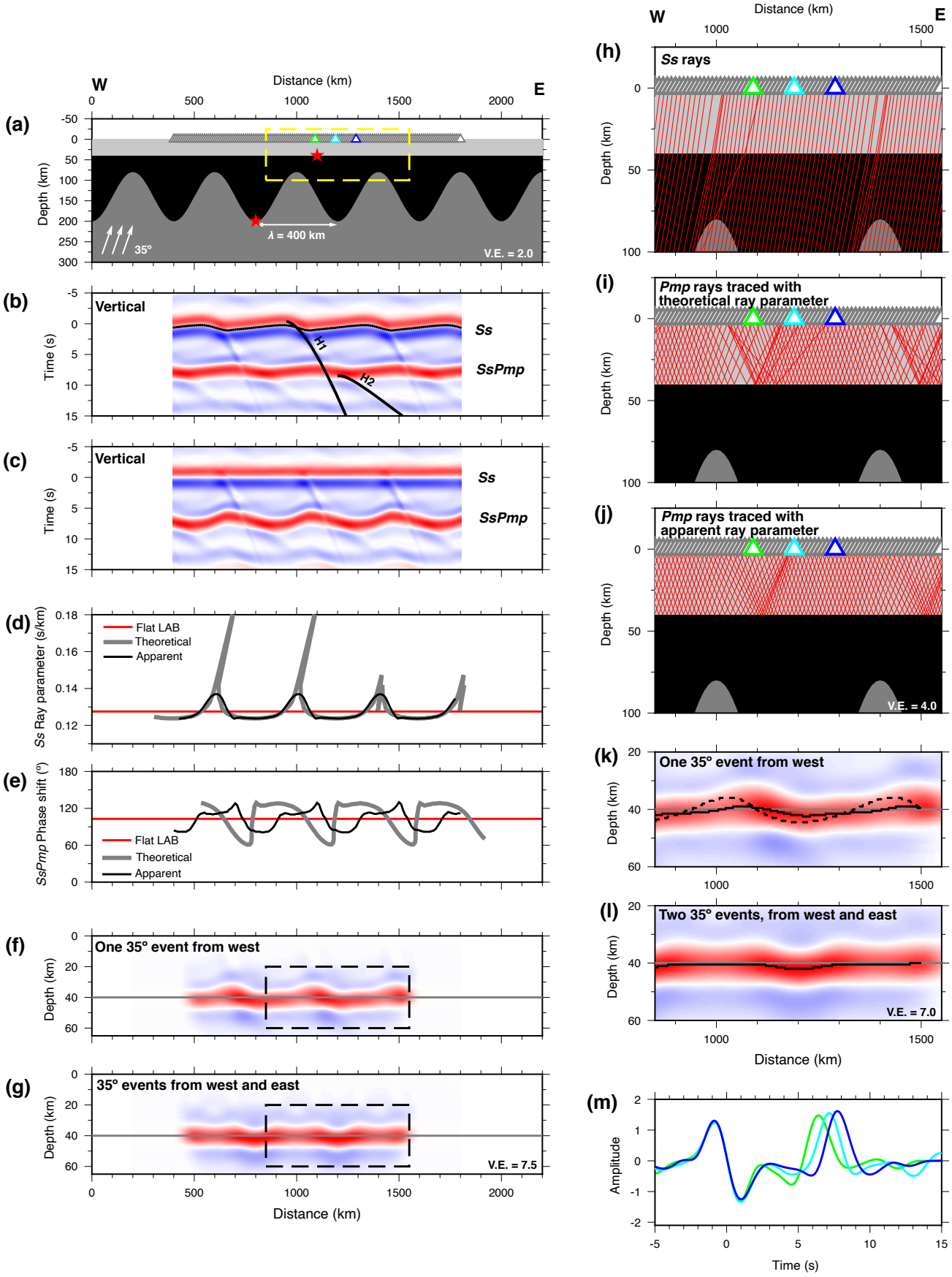
(a)
W
Distance (km)
E
Depth (km)
35°
λ = 400 km
V.E. = 2.0
(b)
Vertical
Time (s)
Ss
SsPmp
H1
H2
(c)
Vertical
Time (s)
Ss
SsPmp
(d)
Ss Ray parameter (s/km)
Flat LAB
Theoretical
Apparent
(e)
SsPmp Phase shift (°)
Flat LAB
Theoretical
Apparent
(f)
One 35° event from west
Depth (km)
(g)
35° events from west and east
Depth (km)
V.E. = 7.5
Distance (km)
(h)
W
Distance (km)
E
Ss rays
Depth (km)
(i)
Pmp rays traced with theoretical ray parameter
Depth (km)
(j)
Pmp rays traced with apparent ray parameter
Depth (km)
V.E. = 4.0
(k)
One 35° event from west
Depth (km)
(l)
Two 35° events, from west and east
Depth (km)
V.E. = 7.0
Distance (km)
(m)
Amplitude
Time (s)

Figure 4. As Fig. 2, now computed with a 400 km-wavelength LAB ($\theta_{av} \sim 31^{\circ}$). H1 and H2: diffraction hyperbolae computed with $H_0 = 200$ km and $V = 4.61$ km/s (H1) and $H_0 = 40$ km and $V = 6.5$ km/s (H2). Red stars: probable diffraction points causing H1 and H2. (g) and (l) are stacked back-projection images of two events with the same incident angle (35º) coming from west and east.

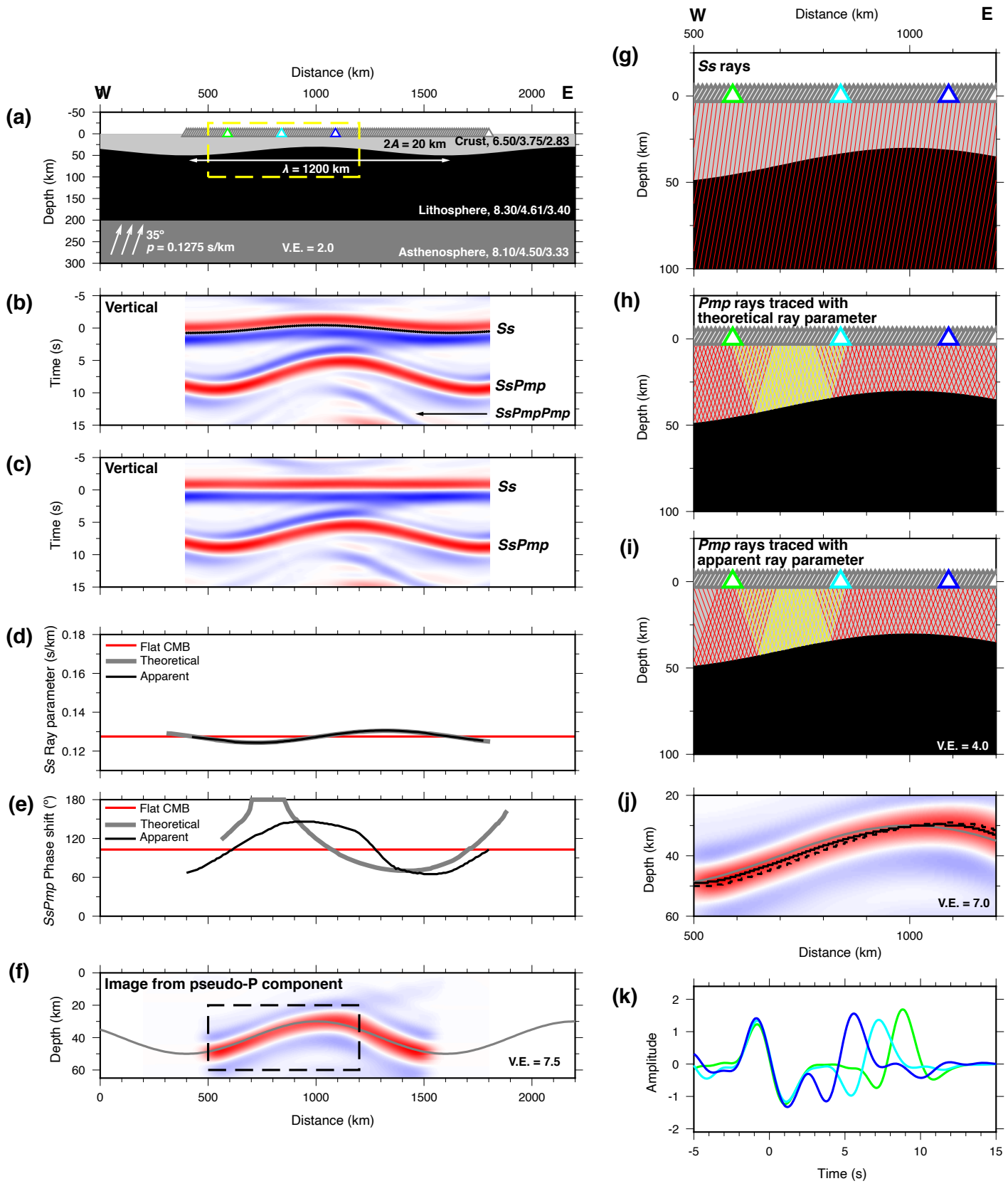
(a)
Distance (km)
W
E
Depth (km)
2A = 20 km
Crust, 6.50/3.75/2.83
λ = 1200 km
Lithosphere, 8.30/4.61/3.40
35°
p = 0.1275 s/km
V.E. = 2.0
Asthenosphere, 8.10/4.50/3.33
(b)
Vertical
Time (s)
Ss
SsPmp
SsPmpPmp
(c)
Vertical
Time (s)
Ss
SsPmp
(d)
Ss Ray parameter (s/km)
Flat CMB
Theoretical
Apparent
(e)
SsPmp Phase shift (°)
Flat CMB
Theoretical
Apparent
(f)
Image from pseudo-P component
Depth (km)
V.E. = 7.5
Distance (km)
(g)
W
Distance (km)
E
Ss rays
Depth (km)
(h)
Pmp rays traced with theoretical ray parameter
Depth (km)
(i)
Pmp rays traced with apparent ray parameter
Depth (km)
V.E. = 4.0
(j)
Depth (km)
V.E. = 7.0
Distance (km)
(k)
Amplitude
Time (s)

Figure 5. As Fig. 2, now computed with a 1200 km-wavelength CMB ($\theta_{av} \sim 2^{\circ}$) and a flat LAB. Yellow rays mark pre-critical reflections at the CMB.

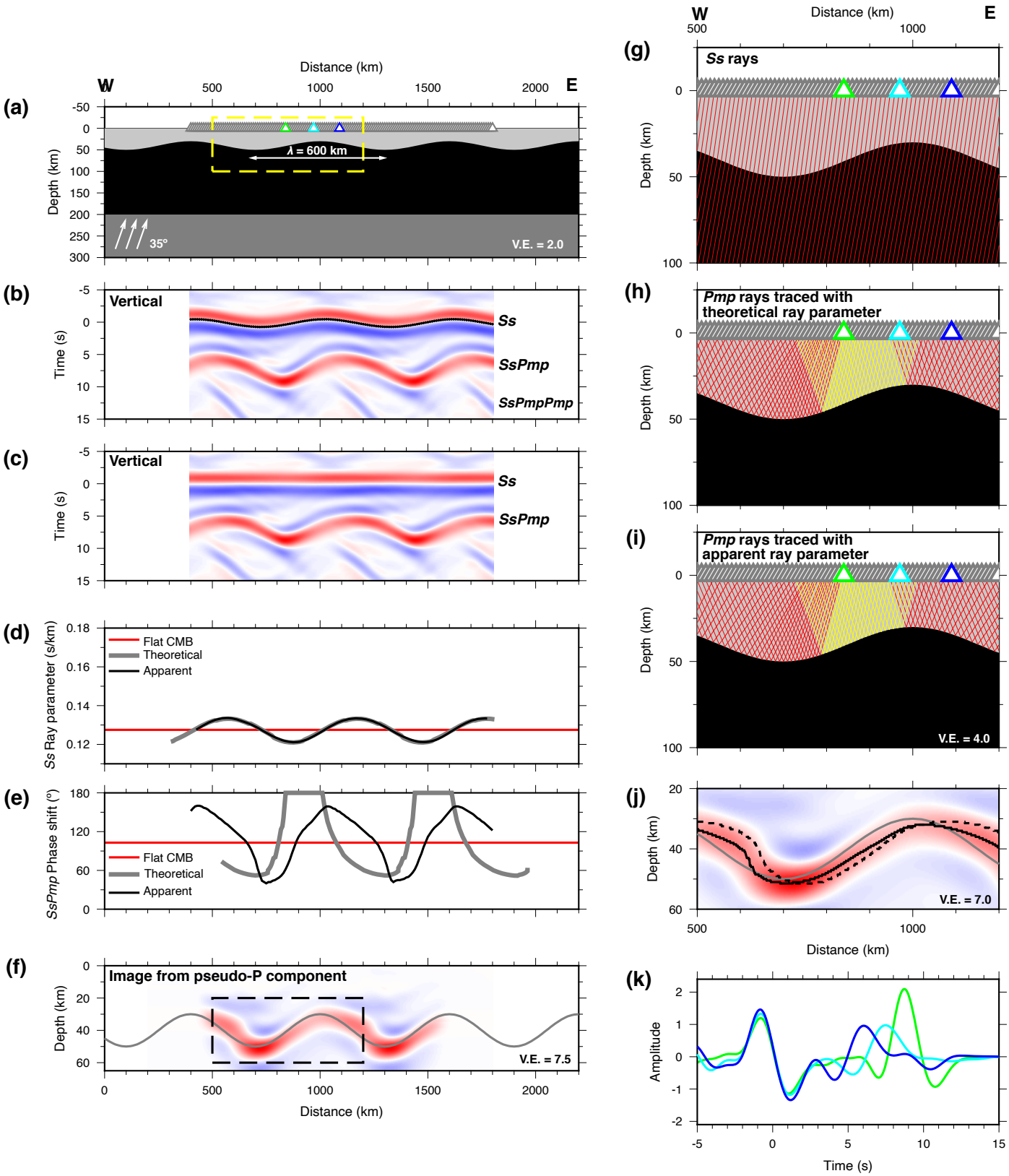
(a)
W
Distance (km)
E
Depth (km)
λ = 600 km
35°
V.E. = 2.0
(b)
Vertical
Time (s)
Ss
SsPmp
SsPmpPmp
(c)
Vertical
Time (s)
Ss
SsPmp
(d)
Ss Ray parameter (s/km)
Flat CMB
Theoretical
Apparent
(e)
SsPmp Phase shift (°)
Flat CMB
Theoretical
Apparent
(f)
Image from pseudo-P component
Depth (km)
V.E. = 7.5
Distance (km)
(g)
W
Distance (km)
E
Ss rays
Depth (km)
(h)
Pmp rays traced with theoretical ray parameter
Depth (km)
(i)
Pmp rays traced with apparent ray parameter
Depth (km)
V.E. = 4.0
(j)
Depth (km)
V.E. = 7.0
Distance (km)
(k)
Amplitude
Time (s)

Figure 6. As Fig. 5, now computed with a 600 km-wavelength CMB ($\theta_{av} \sim 4^{o}$).

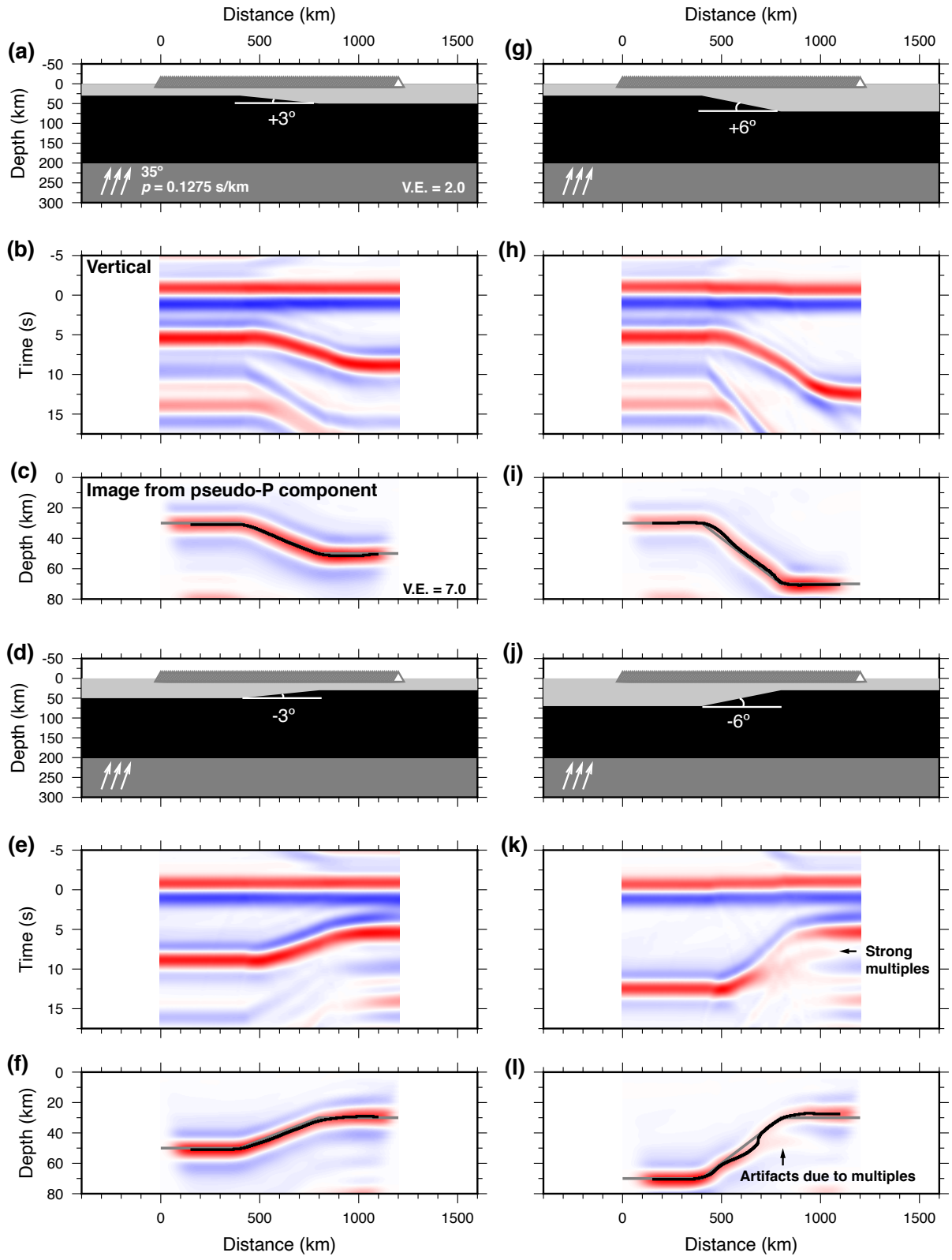
(a)
(b)
(c)
(d)
(e)
(f)
(g)
(h)
(i)
(j)
(k)
(l)
Distance (km)
Depth (km)
Time (s)
+3°
+6°
-3°
-6°
35°
p = 0.1275 s/km
V.E. = 2.0
Vertical
Image from pseudo-P component
V.E. = 7.0
Strong multiples
Artifacts due to multiples

Figure 7. Back-projection images of CMB ramps. (a), (d), (g), and (j) show the models with ±3º- and ±6º-dip ramps respectively. Model parameters for the crust, mantle lithosphere and asthenosphere are the same as all the other cases. Incident angles of the incoming S wave is also 35º. (b), (e), (h), and (k) are the vertical component waveforms computed with the models in (a), (d), (g), and (j) respectively. (c), (f), (i), and (l) show the back-projection images derived from (b), (e), (h), and (k) respectively. Note that the CMB dips are well-recovered in all cases except for a segment in (h) where strong multiples following *SsPmp* cause local artifacts.

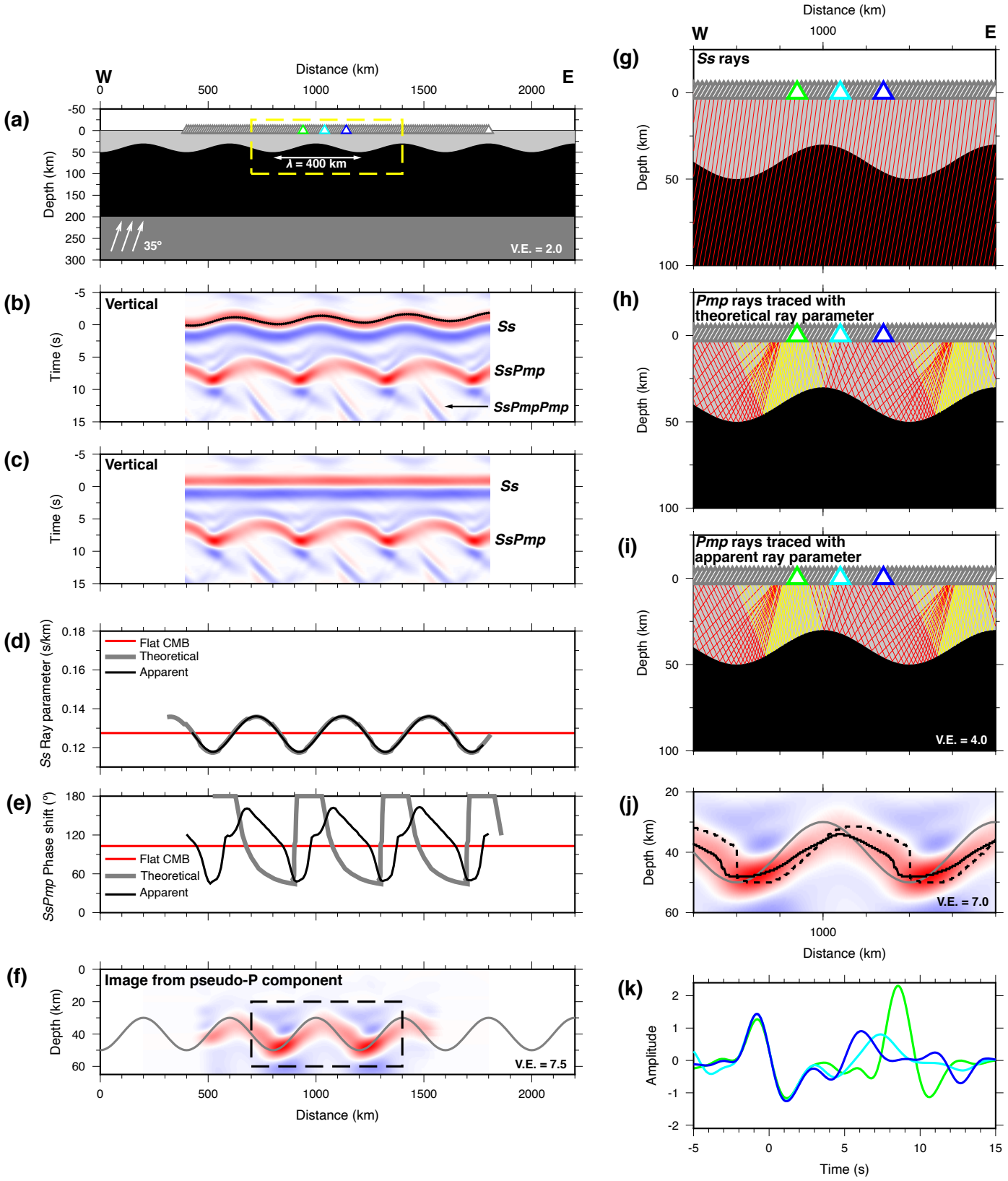
(a)
W
Distance (km)
E
0
500
1000
1500
2000
Depth (km)
λ = 400 km
35°
V.E. = 2.0
(b)
Vertical
Time (s)
Ss
SsPmp
SsPmpPmp
(c)
Vertical
Time (s)
Ss
SsPmp
(d)
Ss Ray parameter (s/km)
Flat CMB
Theoretical
Apparent
(e)
SsPmp Phase shift (°)
Flat CMB
Theoretical
Apparent
(f)
Image from pseudo-P component
Depth (km)
V.E. = 7.5
Distance (km)
(g)
Distance (km)
W
1000
E
Ss rays
Depth (km)
(h)
Pmp rays traced with
theoretical ray parameter
Depth (km)
(i)
Pmp rays traced with
apparent ray parameter
Depth (km)
V.E. = 4.0
(j)
Depth (km)
V.E. = 7.0
1000
Distance (km)
(k)
Amplitude
Time (s)

Figure 8. As Fig. 5, now computed with a 400 km-wavelength CMB ($\theta_{av} \sim 6^{\circ}$).

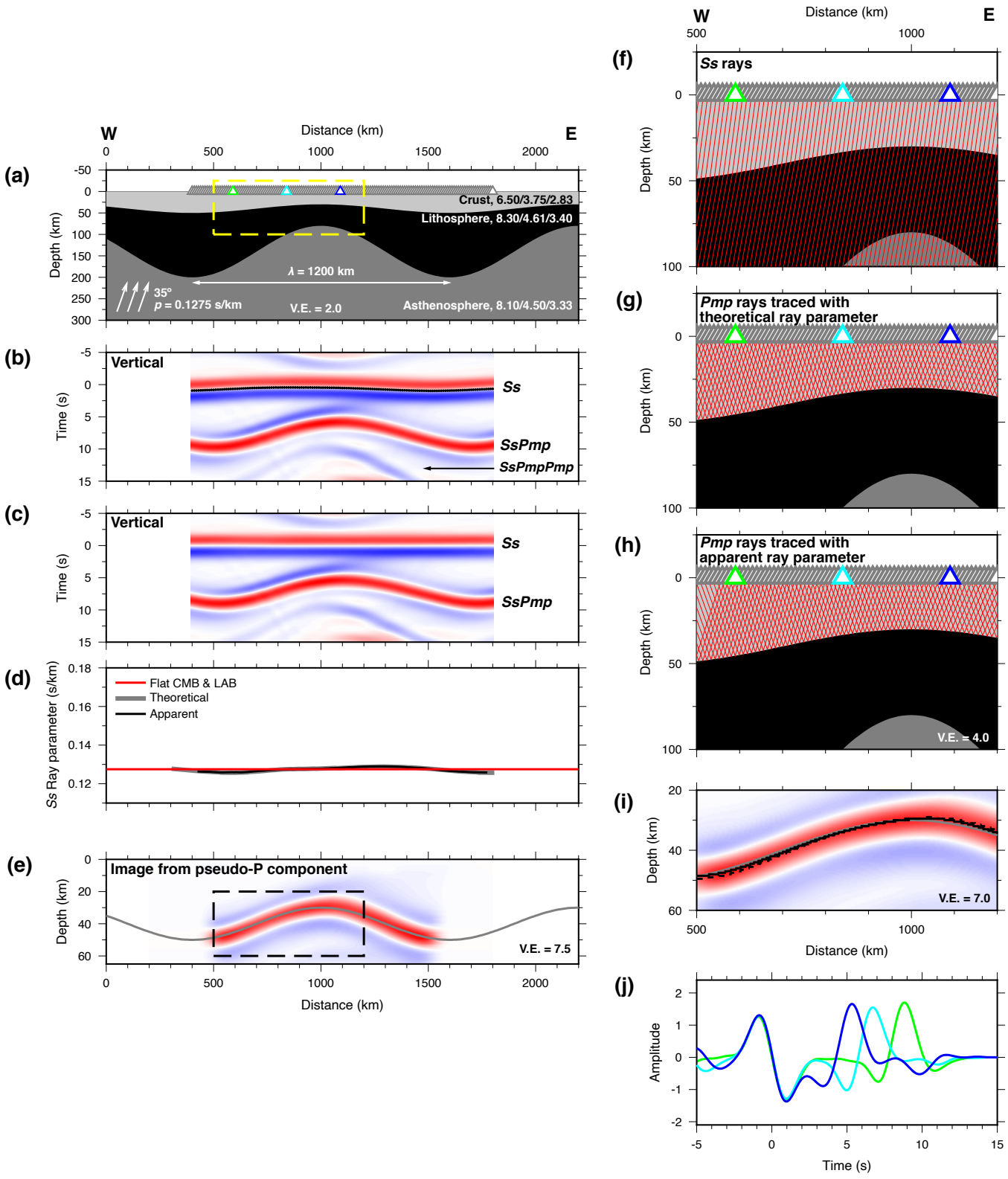

Figure 9. As Fig. 2, now computed with 1200 km-wavelength CMB ($\theta_{av} \sim 2°$) and LAB ($\theta_{av} \sim 11°$).

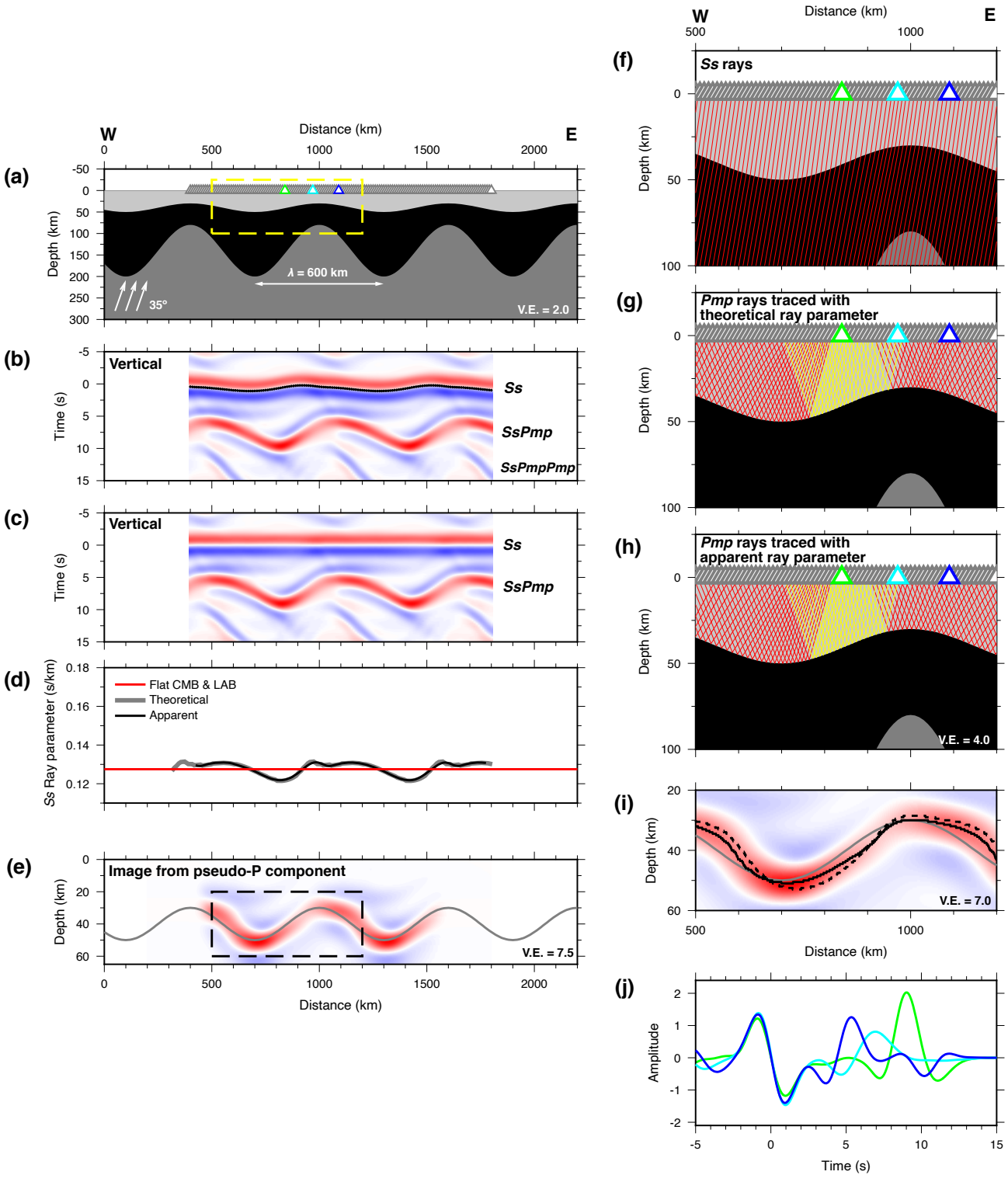

Figure 10. As Fig. 9, now computed with 600 km-wavelength CMB ($\theta_{av} \sim 4°$) and LAB ($\theta_{av} \sim 22°$).

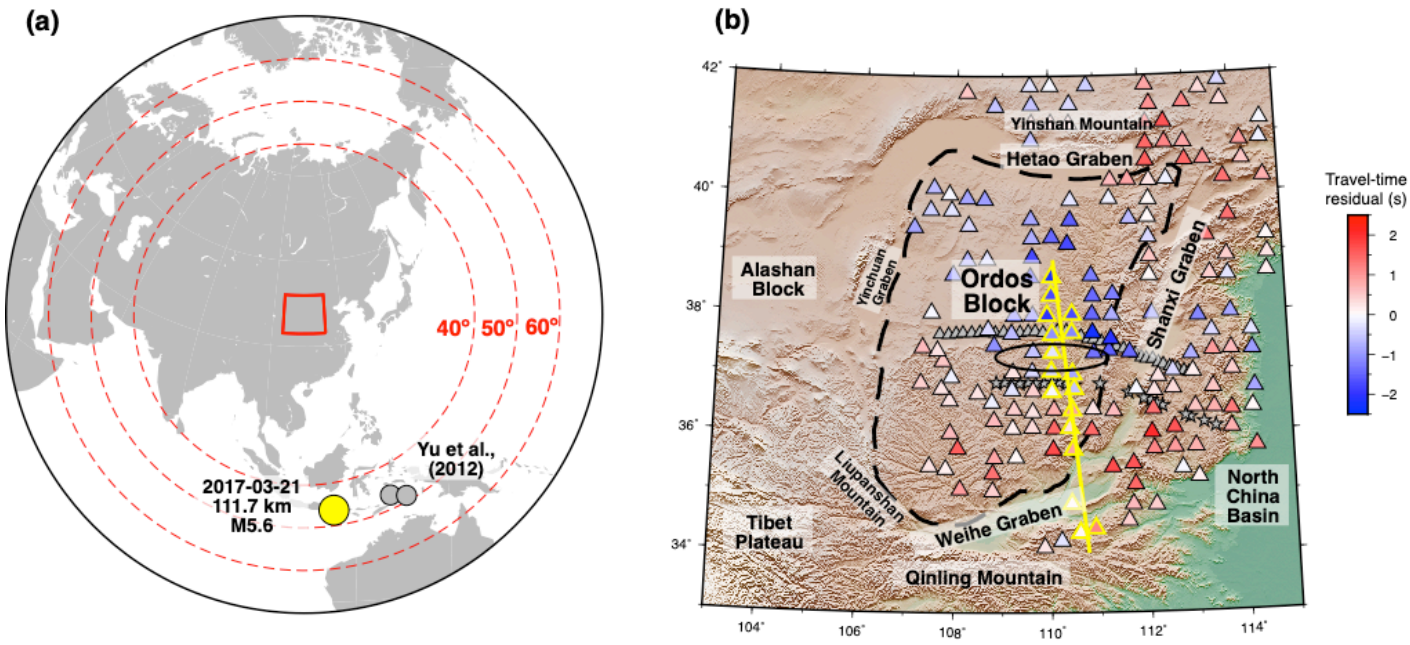

Figure 11. ChinArray over the Ordos Plateau. (a) Study area (red box) and the studied event (yellow circle). Gray circles: events used by Yu et al. (2012). (b) ChinArray stations (2D array recording 2016–2017) and the stations used in Yu et al. (2012) (dense linear array recording 2007–2008). The ChinArray stations are colored by their *Ss* travel-time residuals with respect to the AK135 model. Yellow solid line marks the profile shown in Fig. 13. Stations with yellow edges are the ones within 30 km of, and projected onto the yellow line. Small gray triangles and stars: stations and corresponding virtual sources in Yu et al. (2012). Black oval: approximate range of overthickened crust shown in Yu et al. (2012). Black dashed line: boundary of the Ordos Block.

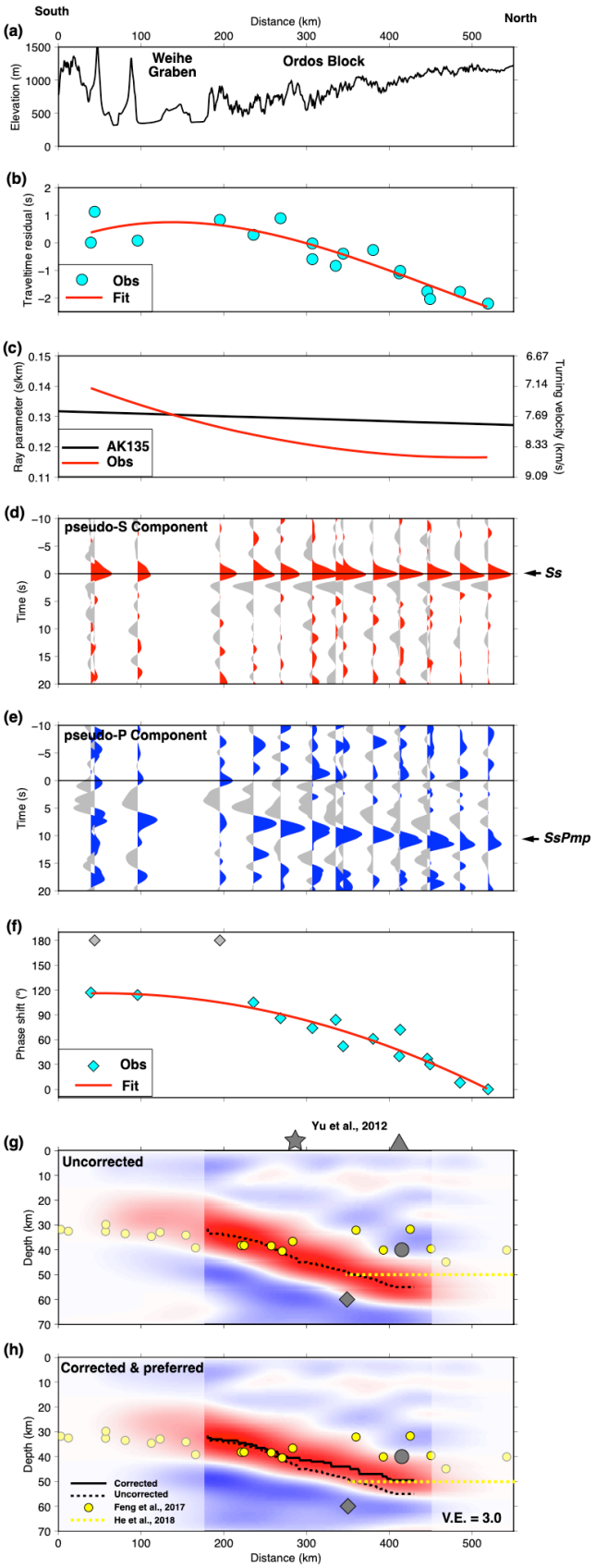
South
North
(a)
Distance (km)
Elevation (m)
Weihe Graben
Ordos Block
(b)
Traveltime residual (s)
Obs
Fit
(c)
Ray parameter (s/km)
Turning velocity (km/s)
AK135
Obs
(d)
pseudo-S Component
Time (s)
Ss
(e)
pseudo-P Component
Time (s)
SsPmp
(f)
Phase shift (°)
Obs
Fit
(g)
Yu et al., 2012
Uncorrected
Depth (km)
(h)
Corrected & preferred
Depth (km)
Corrected
Uncorrected
Feng et al., 2017
He et al., 2018
V.E. = 3.0
Distance (km)

Figure 12. Back projection results using the ChinArray dataset. All profiles are along the yellow line in Fig. 12b. (a) Topography along the profile. (b) *Ss* travel-time residuals along the profile. Cyan circles: *Ss* residuals measured on individual stations. Red curve: travel-time residual along the profile computed by fitting a third-degree polynomial to the measurements. (c) Ray-parameter variation along the profile. Black: ray parameter computed with the AK135 model. Red: observed ray parameter computed by differentiating the fitted travel residual with respect to distance and adding it to the ray-parameter computed with AK135. (d) and (e) pseudo-S-and P-component seismograms recorded at the stations along the profile, aligned to observed *Ss* arrival times. (f) Φ_{VDSS} along the profile. Diamonds: measured Φ_{VDSS} from each pseudo-P component trace along the profile. Cyan diamonds were used to fit the curve; two gray diamonds were excluded. Red curve: Φ_{VDSS} as a function of distance computed by fitting a second-degree polynomial to the observations. (g) and (h) Back-projection images along the profile with x3 vertical exaggeration. Both (g) and (h) are derived with phase-shift of each trace corrected to 0º using the fitted Φ_{VDSS} as a function of distance. V_p^{av} = 6.2 km/s is assumed for both (g) and (h). (g) is computed with zero travel-time residual and the ray parameter predicted by AK135 (uncorrected). (h) is computed with the observed travel-time residuals and ray parameters (corrected & preferred). Solid and dotted black curves: Moho depth picks (maximum amplitude at locations along the profile) for the corrected and uncorrected Moho images (same convention as in the synthetic examples). White translucent rectangles mask areas with less reliable Moho estimations. Gray triangle and star: approximate locations of station and VDSS virtual source respectively from Yu et al. (2012). Gray circle: RF Moho depth from Yu et al. (2012) plotted right below the station. Gray diamond: VDSS Moho depth from Yu et al. (2012) plotted at the approximate reflection point. Yellow circles: RF Moho depth measurements from Feng et al. (2017) on stations within 30 km of the profile. Yellow dotted lines: approximate extent and depth of the bottom of the crustal growth zone from He et al. (2018). Beyond 250 km, the corrected Moho (part h) is significantly shallower than the uncorrected case (part g) and is more consistent with the RF measurements.

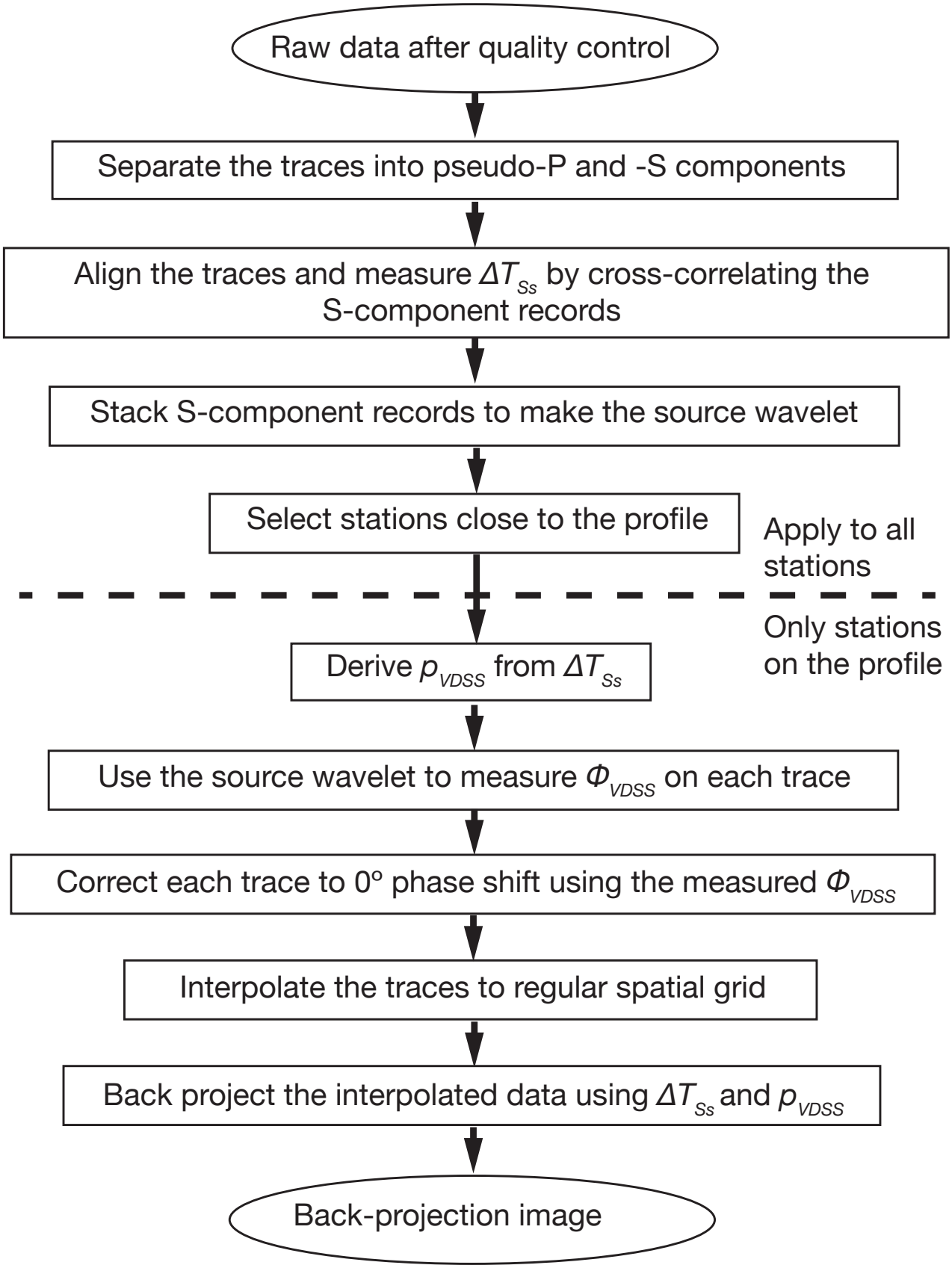

Figure 13. Processing work flow of the Ordos dataset.

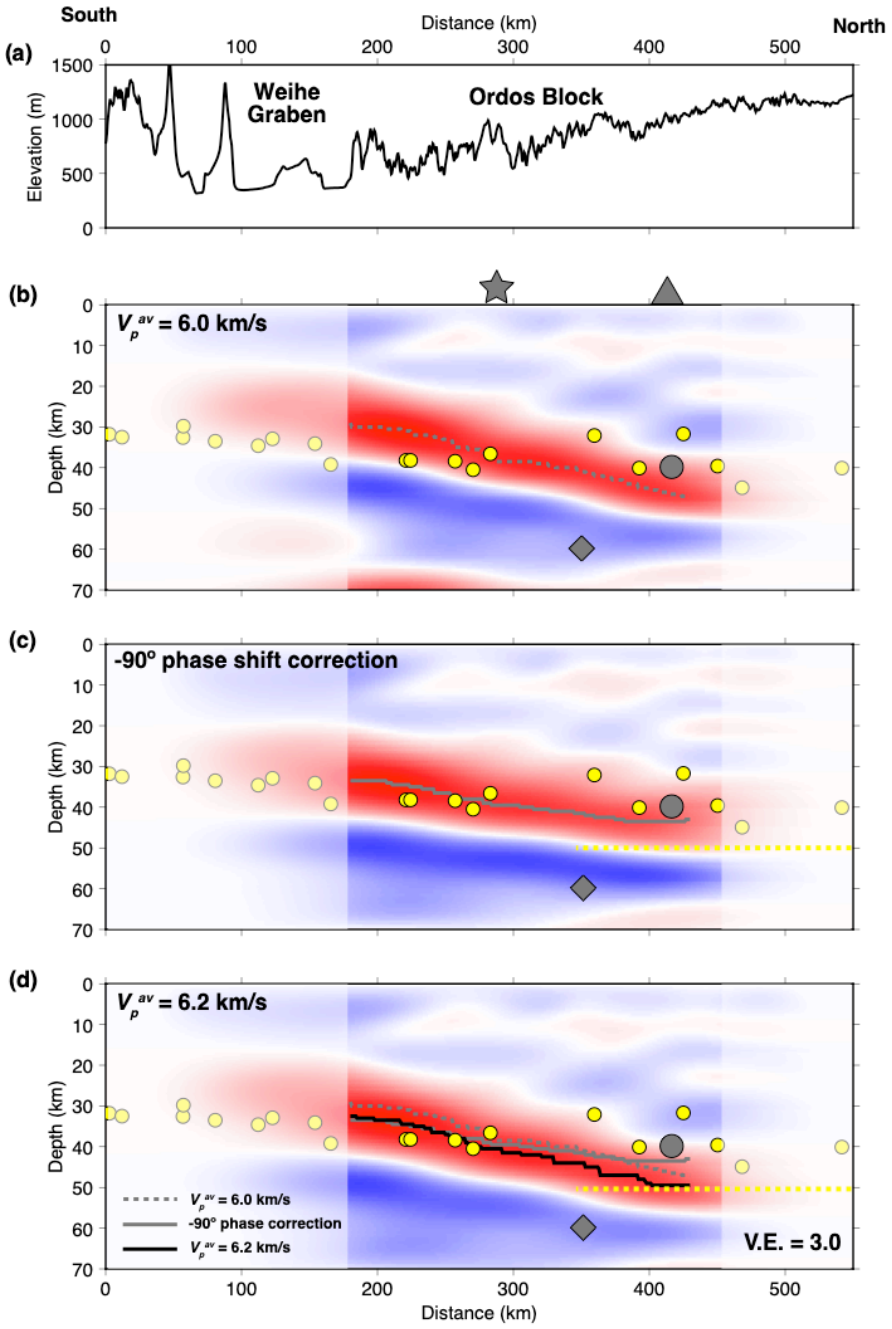

Figure 14. Effects of processing parameters on Moho depth estimations along the profile in Fig. 12. Moho depths from previous studies are denoted as in Fig. 12. (a) The same as Fig. 12a. (b) As Fig. 12h, but computed with V_p^{av} = 6.0 km/s. Gray dotted curve: Moho depth picks. (c) As Fig. 12h, but computed with a -90º-phase-shift correction applied to each trace. Gray solid curve: Moho depth picks. (d) The same as Fig. 12h. Black solid curve: Moho depth picks of this image. Gray dotted and solid curves: Moho depth picks in (b) and (c), respectively.